

ARTICLES

Spin-induced orbital precession and its modulation of the gravitational waveforms from merging binaries

Theocharis A. Apostolatos, Curt Cutler,* Gerald J. Sussman,[†] and Kip S. Thorne
Theoretical Astrophysics, California Institute of Technology, Pasadena, California 91125

(Received 16 February 1994)

Merging compact binaries are currently regarded as the most promising source of gravitational waves for the planned Earth-based LIGO/VIRGO laser-interferometer detector system, and will be an important source also for similar, lower-frequency detectors that might be flown in space (e.g., the proposed LISA mission). During the orbital inspiral, if one or both bodies are rapidly rotating, the general relativistic spin-orbit and spin-spin coupling (i.e., the “dragging of inertial frames” by the bodies’ spins) cause the binary’s orbital plane to precess. In this paper we analyze the resulting modulation of the inspiral gravitational waveform, using post²-Newtonian equations to describe the precession of the orbital plane, but only the leading-order (Newtonian, quadrupole-moment approximation) equations to describe the orbit, the radiation reaction, the inspiral, and the wave generation. We derive all the formulas one needs to readily compute the spin-modulated gravitational waveform (within the post-Newtonian approximation and the approximation that the precession frequency is much smaller than the orbital frequency). We also develop intuition into what the modulated signals “look like,” by a variety of means. We provide approximate, analytical solutions for the precessional motion and the modulated waveforms for two important special cases: the case where the bodies have nearly equal masses and the case where one of the bodies has negligible spin. For these cases, for almost all choices of binary parameters, the motion is a *simple precession* of the orbital angular momentum around the nearly fixed direction of the total angular momentum, with a few tens of precession periods as the waves sweep through the LIGO/VIRGO observational band. However, when the spin and orbital angular momenta are approximately anti-aligned, there is a *transitional-precession* epoch during which their near cancellation causes the binary to “lose its gyroscopic bearings” and tumble in space, with a corresponding peculiar sweep of the waveform modulation. We also explore numerically the precessional behaviors that occur for general masses and spins; these typically appear quite similar to our special-case, simple-precession, and transitional-precession solutions. An Appendix develops several diagrammatic aids for understanding intuitively the relation between the precessing orbit and the modulated waveform.

PACS number(s): 04.80.Nn, 04.30.Db, 97.60.Jd, 97.80.Af

I. INTRODUCTION

Merging compact binaries, i.e., neutron-star–neutron-star (NS-NS), neutron star–black-hole (NS-BH), and black-hole–black-hole (BH-BH) binaries, are currently regarded as the most promising source of gravitational waves for the planned LIGO/VIRGO laser-interferometer detector system [1–3]. LIGO/VIRGO will have good sensitivity in the range $\sim 10\text{--}500$ Hz, and hence will observe the last few minutes and last several thousand cycles of the inspiral waveforms.

To lowest order, the inspiral and the resulting waveform are described by the “Newtonian” quadrupole formula. It has recently been pointed out [3–5] that post-Newtonian corrections to the waveform, though small instantaneously, produce large cumulative effects, which may permit fairly sensitive measurements of certain combinations of the binary’s masses and spins. The cumulative effects are of two types [3]. (i) Post-Newtonian corrections to the binary’s inspiral rate result in a large, secular correction to the phase of the waveform. Details of this accumulating phase correction have been computed by Lincoln and Will [6], Cutler *et al.* [3], Poisson [7], and Kidder, Wiseman, and Will [8], based in part on the earlier work of Wagoner and Will [9], and of Blanchet, Damour, and Iyer [10,11], and the accuracy of the information that LIGO/VIRGO should be able to extract from the accumulating phase correction has been computed by Cutler and Flanagan [4]. (ii) Post-Newtonian spin-orbit and spin-spin couplings cause the orbital plane

*Present address: Center for Radiophysics and Space Research, Cornell University, Ithaca, NY 14853.

[†]Present address: Department of Electrical Engineering, Massachusetts Institute of Technology, Cambridge, MA 02139.

to precess tens of times as the waves sweep through the LIGO/VIRGO band, thereby modulating the waves' amplitude, phase, and polarization [3]. For large spins the effects on the waveform can be quite dramatic, as one can see from a brief perusal of Figs. 5 and 11–18 below.

In this paper we explore in detail the modulation of the waveform due to spin-induced precession. This modulation is qualitatively different from other post-Newtonian effects. Since our principal purpose in this paper is to explore this “new” behavior, we will isolate it by neglecting other post-Newtonian corrections to the waveforms. Most especially, we will neglect other effects of the bodies’ spins, such as their direct wave emission and their contribution, via radiation reaction, to the waves’ cumulative phase correction. These other spin effects have been explored by Kidder, Wiseman, and Will [8], by Kidder [12], and by Cutler and Flanagan [4].

The spin-induced modulation will be important not only for waves from normal-mass compact binaries ($M \sim 1\text{--}10^2 M_\odot$), which lie in the LIGO/VIRGO frequency band, but also for waves emitted by supermassive black-hole binaries ($M \sim 10^3 M_\odot\text{--}10^7 M_\odot$) and by stars and small black holes spiraling into supermassive black holes. These low-frequency waves are targets for laser-interferometer detectors that might be flown in space in the early 21st century, e.g., the proposed LISA (“Laser Interferometer Space Antenna”) mission [13], which is currently the subject of a one-year study funded by the European Space Agency.

The rest of this paper is organized as follows. In Sec. II we briefly review the “lowest-order” waveforms that one calculates from the binary’s time-varying Newtonian quadrupole moment, neglecting spin effects. In Sec. III A we write down the post-Newtonian equations that describe the precession of the orbital plane. In Sec. III B we derive the equations that describe the corresponding modulation of the gravitational waveform, and in Sec. III C we give a simple expression for the Fourier transform of the modulated waveform. In Sec. IV we specialize to two important special cases, for which the precession equations simplify greatly and in the same manner: the case where the bodies have nearly equal masses and the case where one of the bodies has negligible spin. In Sec. IV A we write down and discuss the precession equations for these two cases, neglecting spin-spin coupling (which is of post²-Newtonian order) but keeping spin-orbit coupling (which is of post^{1.5}-Newtonian order). The precession can take two forms: *simple precession* and *transitional precession*. *Simple precession*, which is in some sense the norm, occurs whenever the binary’s total angular momentum vector is not small compared to the orbital or spin angular momenta, i.e., whenever the orbital and spin angular momenta do not conspire to almost cancel each other. In that case, we shall show, the direction of the binary’s total angular momentum vector remains nearly fixed during the inspiral, and the orbital angular momentum vector (i.e., the normal to the orbital plane) precesses about that direction. In Sec. IV B we construct analytic expressions for simple precession and the resulting modulation of the gravitational waves. In Sec. IV C we examine several explicit examples of simple

precession and the corresponding waveforms. In a forthcoming paper [12] Kidder will present an analysis similar to what we present in Secs. IV A, B, and C; his work will differ from, and improve upon, ours by incorporating all the post-Newtonian corrections to the waveform through post^{3/2}-Newtonian order (corrections which we have neglected here for simplicity), in addition to the post^{3/2}-Newtonian and post²-Newtonian precessional effects.

In Sec. IV D, we discuss the breakdown of simple precession due to near cancellation of the orbital and spin angular momenta, and we analyze the resulting *transitional precession* of the orbit (a loss of gyroscopic stability which causes the binary to tumble in space) and the corresponding waveform modulation. In Sec. V we discuss the general case, where the bodies have arbitrary spins and masses. The precession and waveforms in the general case are qualitatively quite similar to the special cases considered in Sec. IV, as we illustrate with several numerical examples. An appendix develops concepts and tools for understanding, intuitively, the amplitude and phase modulation produced by any precession of the orbital plane.

An important question *not* addressed in this paper is how well the modulation can be measured, given realistic detector noise, and how accurately one can thereby measure the bodies’ spins. We plan to address this issue in future work, in a follow-up paper to Ref. [4].

Throughout we use units where $G = c = 1$.

II. NONPRECESSING BINARIES: ORBITAL INSPIRAL AND THE LOWEST-ORDER WAVEFORM

We consider the gravity wave signal measured by a single L-shaped interferometric detector at some location on Earth. We attach a Cartesian coordinate system to the detector, with x and y axes along the detector’s arms and z axis in the vertical direction as shown in Fig. 1. We denote unit vectors along these three axes by $\hat{\mathbf{x}}$, $\hat{\mathbf{y}}$, $\hat{\mathbf{z}}$ and we denote by $\hat{\mathbf{N}}$ the unit vector pointing towards the source binary, and by (θ, ϕ) the spherical polar coordinates of $\hat{\mathbf{N}}$ with respect to our Cartesian coordinates.

To further establish notation, let us review the lowest-order description of the inspiral waveform measured by such a detector; i.e., the “Newtonian, quadrupole-moment approximation” (as given in numerous references, e.g., [14]), which neglects spins, higher multipoles, and other post-Newtonian corrections. We denote by M_1 and M_2 the masses of the binary’s two bodies, and by $\mathbf{r}(t)$ the vector pointing from M_1 to M_2 at retarded time t . We assume the orbital eccentricity is negligible (which will be true if the compact binary was born with orbital period $P \gtrsim 1$ h and the orbit has since decayed due to gravitational radiation reaction [15]). Then the orbital angular momentum is given by

$$\mathbf{L} = \mu M^{1/2} r^{1/2} \hat{\mathbf{L}}, \quad (1)$$

where $M \equiv M_1 + M_2$ is the binary’s total mass, $\mu \equiv$

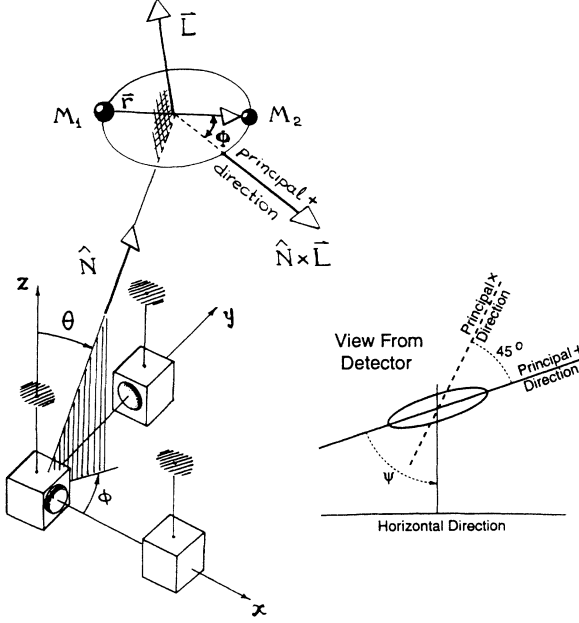


FIG. 1. A Cartesian coordinate system (x, y, z) attached to a gravitational-wave detector, and the geometry of a coalescing binary relative to these coordinates.

$M_1 M_2 / M$ is its reduced mass, $r \equiv |\mathbf{r}|$ is its orbital diameter, and $\hat{\mathbf{L}}$ is the unit vector along \mathbf{L} .

The binary's circular orbit, when projected on the plane of the sky at the detector's location (i.e., projected orthogonal to the waves' propagation direction), looks elliptical; see inset in Fig. 1. The principal axis of this orbital ellipse, which points along $\pm\hat{\mathbf{N}} \times \hat{\mathbf{L}}$, will be called the waves' *principal+* direction; an axis that is rotated counterclockwise from it by 45° in the plane of the sky will be called the waves' *principal×* direction. We resolve the waves into two polarization states: the *principal+* state with polarization axes along and perpendicular to the principal+ direction, and the *principal×* state with polarization axes along and perpendicular to the principal× direction. Any plane-fronted gravitational wave traveling in the $-\hat{\mathbf{N}}$ direction can be written as some linear combination $h_+(t) \times \{\text{principal+ polarization tensor}\}$ plus $h_\times(t) \times \{\text{principal× polarization tensor}\}$, where $h_+(t)$ and $h_\times(t)$ are positive, by convention, whenever the tidal deformations along the principal+ and principal× directions are stretches (as opposed to compressions).

With these conventions, in the Newtonian, quadrupole-moment approximation, the gravitational-wave fields $h_+(t)$ and $h_\times(t)$ are given by

$$h_+(t) = -\frac{2\mu M}{rD} \left[1 + (\hat{\mathbf{L}} \cdot \hat{\mathbf{N}})^2 \right] \cos 2\Phi(t), \quad (2a)$$

$$h_\times(t) = -\frac{2\mu M}{rD} \left[-2\hat{\mathbf{L}} \cdot \hat{\mathbf{N}} \right] \sin 2\Phi(t). \quad (2b)$$

Here D is the distance to the source and $\Phi(t)$ is the angle in the orbital plane from the principal+ direction $\pm\hat{\mathbf{N}} \times \hat{\mathbf{L}}$ to the bodies' separation vector \mathbf{r} ; see Fig. 1. The overall minus sign in Eqs. (2) results from the fact that the

waves' tidal distortion is a squeeze, not a stretch, along the transverse projection of the stars' retarded separation vector $\mathbf{r}(t)$; see the Appendix.

The strain $h(t)$ that the waves produce in the interferometric detector is the following linear combination of $h_+(t)$ and $h_\times(t)$,

$$h(t) = F_+(\theta, \phi, \psi) h_+(t) + F_\times(\theta, \phi, \psi) h_\times(t), \quad (3)$$

where F_+ and F_\times are "detector beam-pattern" coefficients that depend in the following way on the source direction (θ, ϕ) and on a *polarization angle* ψ :

$$F_+(\theta, \phi, \psi) = \frac{1}{2} (1 + \cos^2 \theta) \cos 2\phi \cos 2\psi - \cos \theta \sin 2\phi \sin 2\psi, \quad (4a)$$

$$F_\times(\theta, \phi, \psi) = \frac{1}{2} (1 + \cos^2 \theta) \cos 2\phi \sin 2\psi + \cos \theta \sin 2\phi \cos 2\psi. \quad (4b)$$

The polarization angle ψ (shown in the lower-right inset of Fig. 1) is the angle from the principal+ direction, $\pm\hat{\mathbf{N}} \times \hat{\mathbf{L}}$, clockwise in the plane of the sky to the direction of constant azimuth, $\pm\hat{\mathbf{N}} \times (\hat{\mathbf{N}} \times \hat{\mathbf{z}}) = \pm[-\hat{\mathbf{z}} + \hat{\mathbf{N}}(\hat{\mathbf{N}} \cdot \hat{\mathbf{z}})]$. (The \pm signs are included because ψ is defined only modulo π .) In other words, up to an arbitrary multiple of π ,

$$\psi = \arctan \left(\frac{\hat{\mathbf{L}} \cdot \hat{\mathbf{z}} - (\hat{\mathbf{L}} \cdot \hat{\mathbf{N}})(\hat{\mathbf{z}} \cdot \hat{\mathbf{N}})}{\hat{\mathbf{N}} \cdot (\hat{\mathbf{L}} \times \hat{\mathbf{z}})} \right). \quad (5)$$

[Note: In Figs. 9.2, 9.8, and 9.9 of Ref. [14], ψ is shown with the wrong sign (i.e., opposite to the above). The error is confined to those figures; the equations in Ref. [14] are all in accord with the sign convention used here.]

In the next section we shall divide the precession's modulational effects into an amplitude modulation and a phase modulation. To aid in this, we rewrite the signal strain (3) in the conventional amplitude-and-phase form

$$h(t) = -A(t) \cos[2\Phi(t) + \varphi]. \quad (6)$$

where $A(t)$ and φ (not to be confused with the source's direction angle ϕ) are given by

$$A(t) = \frac{2\mu M}{rD} \left([1 + (\hat{\mathbf{L}} \cdot \hat{\mathbf{N}})^2]^2 F_+^2(\theta, \phi, \psi) + 4[\hat{\mathbf{L}} \cdot \hat{\mathbf{N}}]^2 F_\times^2(\theta, \phi, \psi) \right)^{1/2}, \quad (7a)$$

$$\varphi = \tan^{-1} \left(\frac{2\hat{\mathbf{L}} \cdot \hat{\mathbf{N}} F_\times(\theta, \phi, \psi)}{[1 + (\hat{\mathbf{L}} \cdot \hat{\mathbf{N}})^2] F_+(\theta, \phi, \psi)} \right). \quad (7b)$$

We will refer to φ as the signal's *polarization phase*. We have defined the amplitude-and-phase decomposition 7 with an overall minus sign to emphasize the fact that the waves' tidal distortion is a squeeze, not a stretch, along the transverse projection of the stars' separation vector \mathbf{r} ; cf. the Appendix.

Equations (3)–(7) describe the waves in terms of the direction to the source $\hat{\mathbf{N}}$ [and its polar angles (θ, ϕ) relative to the detector's Cartesian coordinates], the vertical direction $\hat{\mathbf{z}}$ at the detector, the normal $\hat{\mathbf{L}}$ to the binary's orbital plane (and the associated polarization angle ψ),

and the binary's total mass M , reduced mass μ , orbital diameter r , orbital phase Φ , and distance from Earth D . When we ignore the orbital precession, then all of these quantities are constant in time except the orbital diameter $r(t)$ and orbital phase $\Phi(t)$. We obtain $r(t)$ by integrating the inspiral rate $dr/dt = (dE/dt)/(dE/dr)$, where we use the Newtonian expression for the energy, $E = -\frac{1}{2}\mu M/r$, and the energy-loss rate given by the quadrupole formula, $dE/dt = -\frac{32}{5}\mu^2 M^3/r^5$. The (well-known) result is

$$r(t) = \left(\frac{256}{5}\mu M^2\right)^{1/4} (t_c - t)^{1/4}, \quad (8)$$

where t_c is the “collision time” at which (formally) $r \rightarrow 0$.

In the absence of precession, $\dot{\Phi} \equiv d\Phi/dt$ is simply the angular velocity Ω of the two bodies in the orbital plane. However since our definition of Φ depends explicitly on the direction $\hat{\mathbf{L}}$ (cf. Fig. 1), $\dot{\Phi}$ will not be equal to Ω when $\hat{\mathbf{L}}$ is time varying. To deal with this, whether the orbit is precessing or not, we define the *carrier* phase of the waveform by

$$\Phi_C(t) \equiv \int \Omega(t) dt. \quad (9)$$

The term “carrier” is intended to recall the carrier signal used in radio transmission, an analogy that we will make clear below, in Sec. III C.

We find it convenient to specify the constant of integration in Eq. (9) so that $\Phi_C(t_c) \equiv \Phi(t_c)$, whether the orbit is precessing or not. Evaluating the integral in Eq. (9) using $\Omega = M^{1/2}/r^{3/2}$ along with Eq. (8), we find that, to lowest order in M/r ,

$$\Phi_C(t) = \Phi(t_c) - \left[\frac{1}{5} \left(\mu^{3/5} M^{2/5} \right)^{-1} (t_c - t) \right]^{5/8}. \quad (10)$$

To reiterate, if one ignores precession, then $\Phi(t)$ is simply $\Phi_C(t)$.

Spin-induced precession causes one other quantity besides r and Φ to be time dependent in the waveform equations (3)–(7): the direction $\hat{\mathbf{L}}$ of the orbital angular momentum. In the next section we describe the motion of $\hat{\mathbf{L}}$ and the corresponding modulation of the waveform.

III. SPIN-INDUCED PRECESSION AND WAVEFORM MODULATION

A. Equations describing orbital precession and inspiral

We now consider the binary's spin-induced orbital precession. Let the bodies have spin angular momenta \mathbf{S}_1 and \mathbf{S}_2 , respectively. For black holes, there is a strict upper limit on the magnitude of the spins: $|\mathbf{S}_i| \leq M_i^2$. For neutron stars the upper limit is comparable, but depends somewhat on the (uncertain) nuclear equation of state. Most candidate equations of state yield an upper limit of $|\mathbf{S}_i| \lesssim \frac{1}{2}M_i^2$ for uniformly rotating neutron stars [16]. To simplify the discussion, below we will assume $|\mathbf{S}_i| \leq M_i^2$ for all bodies.

Approximate equations of precession for the binary's spins and orbit have been derived in a variety of ways by a number of researchers; see, e.g., Barker and O'Connell [17] for a derivation that assumes gravity is weak throughout the binary, and Hartle and Thorne [18] for a derivation that permits the bodies' internal gravity to be arbitrarily strong but requires their gravitational interaction to be weak. After specializing to circular orbits and after averaging over one orbit, the precession equations take the following form, accurate through post²-Newtonian order:

$$\begin{aligned} \dot{\mathbf{L}} &= \frac{1}{r^3} \left[\frac{4M_1 + 3M_2}{2M_1} \mathbf{S}_1 + \frac{4M_2 + 3M_1}{2M_2} \mathbf{S}_2 \right] \times \mathbf{L} \\ &\quad - \frac{3}{2} \frac{1}{r^3} [(\mathbf{S}_2 \cdot \hat{\mathbf{L}})\mathbf{S}_1 + (\mathbf{S}_1 \cdot \hat{\mathbf{L}})\mathbf{S}_2] \times \hat{\mathbf{L}} \\ &\quad - \frac{32}{5} \frac{\mu^2}{r} \left(\frac{M}{r} \right)^{5/2} \hat{\mathbf{L}}, \end{aligned} \quad (11a)$$

$$\begin{aligned} \dot{\mathbf{S}}_1 &= \frac{1}{r^3} \left[\frac{4M_1 + 3M_2}{2M_1} (\mu M^{1/2} r^{1/2}) \hat{\mathbf{L}} \right] \times \mathbf{S}_1 \\ &\quad + \frac{1}{r^3} \left[\frac{1}{2} \mathbf{S}_2 - \frac{3}{2} (\mathbf{S}_1 \cdot \hat{\mathbf{L}}) \hat{\mathbf{L}} \right] \times \mathbf{S}_1, \end{aligned} \quad (11b)$$

$$\begin{aligned} \dot{\mathbf{S}}_2 &= \frac{1}{r^3} \left[\frac{4M_2 + 3M_1}{2M_2} (\mu M^{1/2} r^{1/2}) \hat{\mathbf{L}} \right] \times \mathbf{S}_2 \\ &\quad + \frac{1}{r^3} \left[\frac{1}{2} \mathbf{S}_1 - \frac{3}{2} (\mathbf{S}_2 \cdot \hat{\mathbf{L}}) \hat{\mathbf{L}} \right] \times \mathbf{S}_2. \end{aligned} \quad (11c)$$

Here an overdot represents “ d/dt ” and to this order of approximation, $r(t)$ is given by Eq. (8) and $L(t) = \mu(Mr)^{1/2}$ [Eq. (1)]. The first square bracketed terms in Eqs. (11a,b,c), which involve just one spin \mathbf{S} , are due to post^{1.5}-Newtonian-order spin-orbit coupling, and the second square-bracketed terms, involving two \mathbf{S} 's, are due to post²-Newtonian-order spin-spin coupling. The last term in $d\mathbf{L}/dt$ [Eq. (11a)] is due to radiation reaction [cf. Eqs. (1) and (8)]; it is the only term that changes the magnitude of any of the angular momenta. Note that the change in the total vectorial angular momentum $\mathbf{J} \equiv \mathbf{L} + \mathbf{S}_1 + \mathbf{S}_2$ is entirely due to this radiation-reaction term; Eqs. (11) imply that

$$\dot{\mathbf{J}} = \dot{\mathbf{L}}^{(\text{react})} = -\frac{32}{5} \frac{\mu^2}{r} \left(\frac{M}{r} \right)^{5/2} \hat{\mathbf{L}}. \quad (12)$$

In Sec. IV, we will derive approximate, analytic solutions for $\hat{\mathbf{L}}(t)$ for special cases. Before doing so, however, we must deal with a few other issues:

In writing the angular-momentum evolution equations in the form (11), we have used the fact that, to lowest order, radiation reaction causes $|\mathbf{L}| = L$ to decrease, but does not affect $|\mathbf{S}_1|$ and $|\mathbf{S}_2|$. Since this fact might not be obvious, we now demonstrate it by computing the leading-order radiation-reaction torque on the binary's bodies. We restrict attention to the radiation reaction torque on body 1; the same argument will apply to body 2. Since our goal is an order of magnitude estimate and not an exact equation, we shall simplify the calculation by treating body 1 formally as a Newtonian-order star, and we shall set $\mu \sim M_1 \sim M_2 \sim M$, and let the radius of

star 1 (which is actually a neutron star or black hole) be of order its gravitational radius, $R_1 \sim M_1 \sim M$, and let the star's spin be of order its maximum allowed value, $S_1 \sim M_1^2 \sim M^2$. The gravitational radiation-reaction potential inside the star is given by [19]

$$\Phi(\text{react}) = \frac{1}{5} \frac{d^5 \mathcal{I}_{jk}}{dt^5} x^j x^k , \quad (13)$$

where \mathcal{I}_{jk} is the binary's quadrupole-moment tensor, and, in order of magnitude,

$$d^5 \mathcal{I}_{jk}/dt^5 \sim \mu r^2 \Omega^5 \sim M^{7/2} r^{-11/2} . \quad (14)$$

Inside star 1 we introduce coordinates $\bar{x}^i \equiv x^i - x_1^i$, where x_1^i is the star's center of mass. Then the radiation reaction acceleration $-\nabla\Phi(\text{react})$ produces a torque τ on star 1 (about its center-of-mass), whose components are

$$\tau^i = -\epsilon^{ijk} \frac{2}{5} \frac{d^5 \mathcal{I}_{kl}}{dt^5} \int (\rho \bar{x}_j \bar{x}^l) dV_1 , \quad (15)$$

where ρ is the star's density, and the integral is taken over star 1. Because tidal distortions of the shape of the star are extremely small (see below), to high accuracy the star is axisymmetric about its spin axis; this symmetry, together with our assumptions that $R_1 \sim M_1 \sim M$ and that the star is rapidly rotating and thus strongly centrifugally flattened, implies that

$$\int (\rho \bar{x}_j \bar{x}^l) dV_1 = M^3 (a \delta_j^l + b \hat{\mathbf{S}}_{1j} \hat{\mathbf{S}}_1^l) \quad (16)$$

for some a and b that are dimensionless and of order unity. The term $a \delta_j^l$ vanishes when contracted into $\epsilon^{ijk} d^5 \mathcal{I}_{kl}/dt^5$, so

$$\begin{aligned} \tau^i &= -\frac{2}{5} b \epsilon^{ijk} \frac{d^5 \mathcal{I}_{kl}}{dt^5} M^3 \hat{\mathbf{S}}_{1j} \hat{\mathbf{S}}_1^l \\ &\sim M^{13/2} r^{-11/2} . \end{aligned} \quad (17)$$

Here, in the second line, we have used Eq. (14). Notice the following: (i) In order of magnitude, the radiation-reaction torque (17) is smaller by $\sim (M/r)^3$, i.e., by three full post-Newtonian orders, than the spin-orbit coupling torque (11b), and smaller by two full orders than the radiation-reaction-induced loss of orbital angular momentum, dL/dt . (ii) The scalar product of the radiation-reaction torque (17) with \mathbf{S}_1 vanishes (by the antisymmetry of ϵ^{ijk}), so at this leading order in the radiation reaction, the magnitude of the body's spin, S_1 , remains constant. (iii) To produce a change in S_1 , the radiation-reaction acceleration must couple to a nonaxisymmetric piece of $\int (\rho \bar{x}_j \bar{x}^l) dV_1$. The dominant deviation from axisymmetry is due to tidal distortion by the gravity of the star's companion, and it is smaller by $(M/r)^3$ than the axisymmetric part of $\int (\rho \bar{x}_j \bar{x}^l) dV_1$. Correspondingly, the S_1 -changing piece of the radiation-reaction torque will be a full five post-Newtonian orders smaller than dL/dt , and we can safely ignore it.

The spin-up of the bodies due to tidal interactions is also negligible for the cases of interest to us, as shown by Bildsten and Cutler [20].

B. Equations describing the modulation of the waveform

In this section we describe the modulation of the waveform caused by the orbital precession. A key point is that (as we show below) the orbital period is much shorter than the timescale for $\hat{\mathbf{L}}$ to change significantly; i.e., $\hat{\mathbf{L}}$ is roughly constant over many gravity wave cycles. Therefore to a good approximation we can simply take over the expressions (2)–(7) for the wave fields $H_+(t)$ and $h_\times(t)$, and the detector-measured waveform amplitude $A(t)$ and polarization phase $\varphi(t)$, but plug into those expressions the time-varying $\hat{\mathbf{L}}(t)$ obtained by solving the precession equations (11). This approximation will be correct up to terms of order the precession frequency over the gravity wave frequency.

Note that the expressions for $h_+(t)$, $h_\times(t)$, $A(t)$, and $\varphi(t)$ in Eqs. (3)–(7) depend on $\hat{\mathbf{L}}(t)$ explicitly through the $\hat{\mathbf{L}} \cdot \hat{\mathbf{N}}$ terms and implicitly through ψ . Thus, to be completely explicit, our precession-modulated fields and gravitational waveform are

$$h_+(t) = -\frac{2\mu M}{rD} \left[1 + (\hat{\mathbf{L}}(t) \cdot \hat{\mathbf{N}})^2 \right] \cos 2\Phi(t) , \quad (18a)$$

$$h_\times(t) = -\frac{2\mu M}{rD} \left[-2\hat{\mathbf{L}}(t) \cdot \hat{\mathbf{N}} \right] \sin 2\Phi(t) , \quad (18b)$$

$$h(t) = -A(t) \cos[2\Phi(t) + \varphi(t)] , \quad (18c)$$

where

$$\begin{aligned} A(t) &= \frac{2\mu M}{rD} \left([1 + (\hat{\mathbf{L}}(t) \cdot \hat{\mathbf{N}})^2]^2 F_+^2(\theta, \phi, \psi(t)) \right. \\ &\quad \left. + 4[\hat{\mathbf{L}}(t) \cdot \hat{\mathbf{N}}]^2 F_\times^2(\theta, \phi, \psi(t)) \right)^{1/2} , \end{aligned} \quad (19a)$$

$$\varphi(t) = \arctan^{-1} \left(\frac{2\hat{\mathbf{L}}(t) \cdot \hat{\mathbf{N}} F_\times(\theta, \phi, \psi(t))}{[1 + (\hat{\mathbf{L}}(t) \cdot \hat{\mathbf{N}})^2] F_+(\theta, \phi, \psi(t))} \right) , \quad (19b)$$

and where

$$\psi(t) = \arctan \left(\frac{\hat{\mathbf{L}}(t) \cdot \hat{\mathbf{z}} - (\hat{\mathbf{L}}(t) \cdot \hat{\mathbf{N}})(\hat{\mathbf{z}} \cdot \hat{\mathbf{N}})}{\hat{\mathbf{N}} \cdot (\hat{\mathbf{L}}(t) \times \hat{\mathbf{z}})} \right) . \quad (20)$$

Intuitive, diagrammatic methods for visualizing the $\hat{\mathbf{L}}(t)$ -induced modulation of A and φ , for the special cases where the source is directly underfoot or overhead, are given in the Appendix.

In addition to the modulation of the polarization phase φ discussed above, there is an additional modulation of the waveform phase due to an effect which is akin to the Thomas precession of the electron's spin in a semiclassical model of the hydrogen atom. Recall that in Sec. II we introduced a distinction between the carrier phase $\Phi_C(t)$ defined as the integral $\int \Omega dt$ of the bodies' angular velocity in the orbital plane, and $\Phi(t)$, defined as the angle between the orbital separation vector $\hat{\mathbf{r}}$ and the principal+ direction $\pm \hat{\mathbf{L}} \times \hat{\mathbf{N}}$. [The latter definition was required in order for Eqs. (2) for $h_+(t)$ and $h_\times(t)$ to be valid.] We emphasize that we are *not* presently concerned with corrections to the waveform phase $\Phi(t)$ that are due to post-Newtonian corrections to $\Omega(r)$ or $\dot{\Omega}(r)$. Rather,

we are calculating that correction to $\Phi(t)$ which arises from the changing orientation of the orbital plane, *even if we take Ω and $\hat{\Omega}$ to have their lowest-order, “Newtonian” values.* We define the precessional correction to the orbital phase $\delta\Phi(t)$ by

$$\Phi(t) \equiv \Phi_C(t) + \delta\Phi(t), \quad (21)$$

and we now proceed to find an expression for $\delta\Phi$ in terms of $\hat{\mathbf{L}}(t)$.

By definition, the unit orbital separation vector is

$$\hat{\mathbf{r}} = \cos\Phi(t)\hat{\zeta} + \sin\Phi(t)\hat{\mathbf{L}} \times \hat{\zeta}, \quad (22)$$

where

$$\hat{\zeta} \equiv \frac{\hat{\mathbf{L}} \times \hat{\mathbf{N}}}{[1 - (\hat{\mathbf{L}} \cdot \hat{\mathbf{N}})^2]^{1/2}} \quad (23)$$

is the principal+ direction. We also have

$$\dot{\hat{\mathbf{r}}} = \Omega \hat{\mathbf{L}} \times \hat{\mathbf{r}} - (\dot{\hat{\mathbf{L}}} \cdot \hat{\mathbf{r}}) \hat{\mathbf{L}}. \quad (24)$$

The first term on the right side of Eq. (24) rotates $\hat{\mathbf{r}}$ about $\hat{\mathbf{L}}$, while the second term ensures that $\hat{\mathbf{r}}$ remains orthogonal to $\hat{\mathbf{L}}$; the second term basically corresponds to “Fermi-Walker transport” of $\hat{\mathbf{r}}$ due to the precession of the orbital plane. From Eq. (22) we have

$$\cos\Phi(t) = \hat{\zeta} \cdot \hat{\mathbf{r}}. \quad (25)$$

Taking d/dt of Eq. (25) and using Eqs. (22) and (24), we obtain

$$\begin{aligned} -\dot{\Phi}\sin\Phi &= \dot{\hat{\zeta}} \cdot \hat{\mathbf{r}} + \hat{\zeta} \cdot \dot{\hat{\mathbf{r}}} \\ &= \dot{\hat{\zeta}} \cdot \hat{\mathbf{r}} - \Omega\sin\Phi \end{aligned} \quad (26)$$

or [from Eqs. (21) and (9)]

$$\delta\dot{\Phi} = -\dot{\hat{\zeta}} \cdot \hat{\mathbf{r}}/\sin\Phi. \quad (27)$$

Using the definition (23) of $\hat{\zeta}$ and expression (22) for $\hat{\mathbf{r}}$, a few lines of algebra allow us to rewrite Eq. (27) as

$$\delta\dot{\Phi} = \left(\frac{\hat{\mathbf{L}} \cdot \hat{\mathbf{N}}}{1 - (\hat{\mathbf{L}} \cdot \hat{\mathbf{N}})^2} \right) (\hat{\mathbf{L}} \times \hat{\mathbf{N}}) \cdot \dot{\hat{\mathbf{L}}}. \quad (28)$$

This equation must be integrated subject to the boundary condition that $\delta\Phi = 0$ at the end point of the coalescence [Eq. (10) and associated discussion]; therefore,

$$\delta\Phi(t) = - \int_t^{t_c} \left(\frac{\hat{\mathbf{L}} \cdot \hat{\mathbf{N}}}{1 - (\hat{\mathbf{L}} \cdot \hat{\mathbf{N}})^2} \right) (\hat{\mathbf{L}} \times \hat{\mathbf{N}}) \cdot \dot{\hat{\mathbf{L}}} dt. \quad (29)$$

This integral cannot be expressed in terms of $\hat{\mathbf{N}}$ and the instantaneous value of $\hat{\mathbf{L}}$ at time t ; it depends on the full time history of $\hat{\mathbf{L}}$ between times t and t_c [as one can readily verify by expressing the integrand as $\mathbf{F} \cdot d\hat{\mathbf{L}}$ and then noting that the curl of \mathbf{F} (in $\hat{\mathbf{L}}$ space) is nonzero].

In summary, our precession-modulated waveform is

$$h(t) = -A(t) \cos[2\Phi_C(t) + 2\delta\Phi(t) + \varphi(t)]. \quad (30)$$

Here $\Phi_C(t)$ is the integral of $\Omega(t)$, which is given to lowest (Newtonian) order by Eq. (10). To determine $A(t)$, $\varphi(t)$, and $\delta\Phi(t)$ one solves Eqs. (11a)–(11c) for $\hat{\mathbf{L}}(t)$ and plugs the result into Eqs. (19), (20), and (29).

We note that $\delta\Phi(t)$ depends on $\hat{\mathbf{L}}(t)$ and the location of the binary on the sky, but is independent of the orientation of the detector arms. By contrast, $A(t)$ and $\varphi(t)$ do depend on the detector orientation, through the terms F_+ and F_\times in Eqs. (19).

C. Fourier transform of the modulated signal

In this section we derive a simple expression for the Fourier transform of the precession-modulated signal,

$$\tilde{h}(f) \equiv \int_{-\infty}^{+\infty} df e^{2\pi ift} h(t). \quad (31)$$

This is useful for the following reason. The process of searching for a merging-binary waveform $h(t)$ in LIGO/VIRGO data will consist of beating the “Wiener-filtered” version of the waveform, $h_W(t)$, against the measured detector strain $s(t)$, i.e., taking the inner product

$$\int_{-\infty}^{+\infty} s(t) h_W(t) dt. \quad (32)$$

Here the Wiener-filtered waveform $h_W(t)$ is defined by the equation

$$\tilde{h}_W(f) \equiv \tilde{h}(f)/S_h(f), \quad (33)$$

where $S_h(f)$ is the spectral density of the detector noise. (We refer the reader to Ref. [14] for the definition of $S_h(f)$ and for a discussion of noise sources in the LIGO/VIRGO detectors, and to Ref. [1] for estimates of $S_h(f)$ in the first LIGO detectors and more advanced LIGO detectors.)

Radio transmission provides a useful analogy for an intuitive understanding of signal modulation. The unmodulated signal is like the radio station’s high-frequency *carrier* signal, while the effect of precession on the gravity waveform is like the modulation. [The analogy becomes better in the limit that the smaller mass $M_2 \rightarrow 0$, since then the inspiral rate also approaches zero and (the quadrupole piece of) the unmodulated “carrier” waveform becomes truly monochromatic.] In this spirit, let us define a complex “carrier” signal $h_C(t)$ by

$$h_C(t) \equiv \frac{M_1 M_2}{D r(t)} e^{-2i\Phi_C(t)}, \quad (34)$$

where $\Phi_C(t) = \int \Omega dt$ is the carrier phase we defined in Eqs. (9) and (10). The Fourier transform of the carrier signal can be calculated approximately using the stationary phase method, which yields

$$\tilde{h}_C(f) \approx \begin{cases} \frac{M_1 M_2}{D r(t)} (idf/dt)^{-1/2} e^{i[2\pi f t - 2\Phi_C(t)]} & \text{for } f > 0 \\ 0 & \text{for } f < 0, \end{cases} \quad (35)$$

where $t \equiv t(f)$ is the time at which the carrier frequency,

$\dot{\Phi}_C/\pi = \Omega/\pi$, equals f . The difference between expression (35) and the actual Fourier transform of $h_C(t)$ is of the order of the ratio of orbital period to inspiral timescale, which is negligible for cases of interest.

We next define a complex modulation factor

$$\Lambda(t) \equiv A(t) \left[\frac{M_1 M_2}{D r(t)} \right]^{-1} e^{-i[2\delta\Phi(t) + \varphi(t)]}. \quad (36)$$

Then $h(t) = \text{Re} [\Lambda(t) \tilde{h}_C(t)]$. Since $\Lambda(t)$ varies much more slowly than $2\Phi_C(t)$, we can again use the stationary phase method to approximate $\tilde{h}(f)$; the result is

$$\tilde{h}(f) \approx \begin{cases} \frac{1}{2} \Lambda(t(f)) \tilde{h}_C(f) & \text{for } f > 0 \\ \frac{1}{2} \Lambda^*(t(|f|)) \tilde{h}_C^*(|f|) & \text{for } f < 0. \end{cases} \quad (37)$$

The factor $\frac{1}{2}$ in Eq. (37) arises because the real and imaginary parts of $\Lambda(t) \tilde{h}_C(t)$ contribute equally to the Fourier transform, in the stationary phase approximation.

The stationary phase result given above [Eq. (37)] differs from the true $\tilde{h}(f)$ by terms of order the ratio of the orbital period to the precession period; i.e., the stationary phase method computes $\tilde{h}(f)$ less accurately than $\tilde{h}_C(f)$, because the precession time scale is much shorter than the inspiral time scale. We can improve our calculation of $\tilde{h}(f)$ as follows. The stationary phase results quoted above can be viewed as merely the lowest-order results in a power series expansion for the true Fourier transform, where the expansion parameter is the ratio of the orbital period to the precession period. We improve Eq. (37) by adding the next-order term in the expansion; the result is

$$\tilde{h}(f) \approx \frac{1}{2} \Lambda(t) \tilde{h}_C(f) + \frac{1}{4\pi i} \frac{d\Lambda}{dt} \left[\frac{d\tilde{h}_C(f)}{df} - 2\pi i t \tilde{h}_C(f) \right] \quad (38)$$

for positive f , and the complex conjugate of this for negative f . Here, again, $t = t(f)$ is the time at which the carrier frequency Ω/π is equal to f . The formula given in Eq. (38) differs from the true $\tilde{h}(f)$ by terms of order (orbital period/inspiral time scale) and terms of order (orbital period/precession period)².

In this paper, for simplicity, we use only the lowest-order version of the carrier signal $h_C(t)$, and our derivation of $\Lambda(t)$ is of similarly low order. However, our formula (38) has the virtue that it can be applied essentially without modification to versions of $h_C(t)$ and $\Lambda(t)$ that are correct to higher post-Newtonian order. One just plugs the more accurate versions of $\tilde{h}_C(f)$ and $\Lambda(t)$ into Eq. (38), while also using an improved version of $t(f)$. [Actually, the above statement applies only to the dominant, mass-quadrupole piece of the waveform. If one includes the radiation due to the binary's time-varying current-quadrupole and mass-octupole moments (or other, higher-order moments) then the situation is somewhat more complicated, since different moments emit gravitational radiation at different harmonics of the orbital frequency, and their contributions to h_+

and h_x have different dependences on $\hat{\mathbf{L}} \cdot \hat{\mathbf{N}}$ than those given in Eqs. (2).]

IV. BINARIES WITH $M_1 \simeq M_2$ OR $S_2 \simeq 0$

A. Orbital evolution equations, and approximate description of the evolution

In this section we construct approximate, analytic solutions of the inspiral and precession equations (11) for two important special cases: (1) $M_1 = M_2$ and (2) $\mathbf{S}_2 = 0$. Both cases are of interest. The prototypical example where $M_1 \simeq M_2$ would be an NS/NS merger, since measured neutron star masses all cluster near $1.4M_\odot$. The prototypical example where \mathbf{S}_2 can be neglected would be a neutron star spiraling into a much larger, rapidly rotating black hole. In that case, the black-hole spin \mathbf{S}_1 will dominate the orbital precession unless \mathbf{S}_1 is nearly parallel or antiparallel to \mathbf{L} .

Our first approximation is that *we neglect the spin-spin terms in the $M_1 = M_2$ case*. These neglected terms are of post²-Newtonian order and thus will typically be small compared to the post^{3/2}-Newtonian spin-orbit terms, which we retain. Given this approximation, the orbital evolution equations (11) imply that $\mathbf{S}_1 \cdot \mathbf{S}_2$ is constant in time and therefore the total spin vector

$$\mathbf{S} \equiv \mathbf{S}_1 + \mathbf{S}_2 \quad (39)$$

has constant magnitude. Then, *for both of our special cases*, the inspiral and precession equations (11) can be brought into the simple form

$$\dot{L} = \frac{-32 \mu^2}{5} \left(\frac{M}{r} \right)^{5/2}, \quad (40a)$$

$$\dot{S} = 0, \quad (40b)$$

$$\dot{\hat{\mathbf{L}}} = \left(2 + \frac{3M_2}{2M_1} \right) \frac{\mathbf{J}}{r^3} \times \hat{\mathbf{L}}, \quad (40c)$$

$$\dot{\hat{\mathbf{S}}} = \left(2 + \frac{3M_2}{2M_1} \right) \frac{\mathbf{J}}{r^3} \times \hat{\mathbf{S}}. \quad (40d)$$

Here

$$\mathbf{J} = \mathbf{L} + \mathbf{S} \quad (41a)$$

is the binary's total angular momentum and

$$S = |\mathbf{S}| \quad \text{and} \quad \hat{\mathbf{S}} = \mathbf{S}/S \quad (41b)$$

are the magnitude and direction of the total spin.

Let us first describe qualitatively the solutions of the evolution equations (40). The orbital evolution can be divided into two pieces: (1) a precession of the plane containing \mathbf{L} and \mathbf{S} , and (2) the motion of these vectors in this plane. The in-plane evolution is driven by the radiation-reaction-induced orbital shrinkage. This shrinkage causes the length L of \mathbf{L} to decrease, but leaves constant the length S of \mathbf{S} [Eq. (40b)] and the angle $\arccos(\hat{\mathbf{L}} \cdot \hat{\mathbf{S}})$ between \mathbf{L} and \mathbf{S} [cf. Eqs. (40c,d)]. This evolution is depicted in Fig. 2. Note that the angle be-

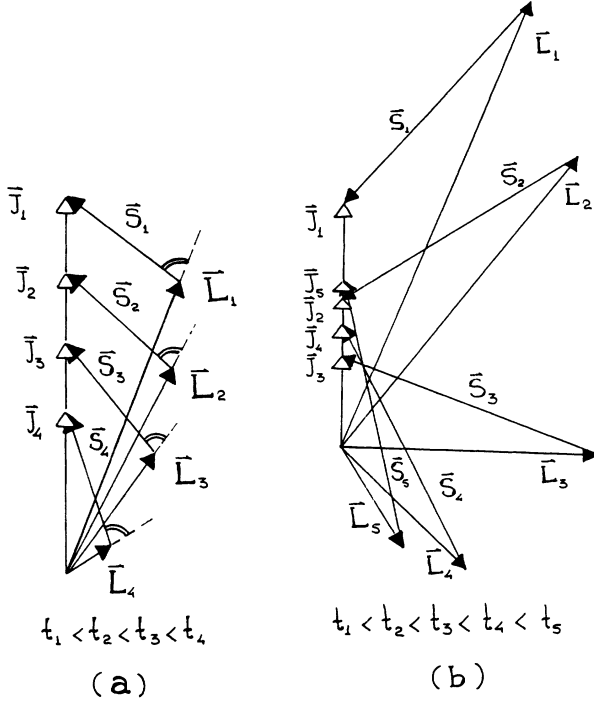


FIG. 2. The in-plane evolution of the total spin angular momentum \mathbf{S} , orbital angular momentum \mathbf{L} and total angular momentum \mathbf{J} for binaries governed by Eqs. (40). When \mathbf{L} and \mathbf{S} are nearly oppositely directed as in drawing (b), the precession initially is simple, then at times $t \sim t_3$ it becomes transitional, then returns to simple. In case (a), the precession is always simple.

tween \mathbf{L} and \mathbf{J} must continually increase.

The precession of the plane containing \mathbf{L} and \mathbf{S} can take one of two qualitatively different forms, which we shall call *simple precession* and *transitional precession*. We shall devote four paragraphs to simple precession, and then shall describe transitional precession.

In *simple precession*, $\hat{\mathbf{S}}$ and $\hat{\mathbf{L}}$ both precess around $\hat{\mathbf{J}}$ with an angular velocity

$$\Omega_p = \left(2 + \frac{3M_2}{2M_1} \right) \frac{J}{r^3} \quad (42)$$

[cf. Eqs. (40c,d)] that is fast compared to the orbital inspiral rate \dot{L}/L . Because \mathbf{L} precesses around $\hat{\mathbf{J}}$, the value of

$$\dot{\mathbf{J}} = \dot{L}\hat{\mathbf{L}} \quad (43)$$

[cf. Eqs. (40)], averaged over one precession, is nearly parallel to \mathbf{J} , and therefore to a reasonable approximation \mathbf{J} changes in magnitude but not in direction; this approximation becomes exact in the limit that $\dot{L}/(\Omega_p J) \rightarrow 0$.

We can integrate Eq. (42) to obtain a back-of-the-envelope estimate of the number of precessions in the observable inspiral, and to see how the precession rate scales with the frequency of the emitted gravity waves. We define the precession angle α by

$$d\alpha/dt = \Omega_p. \quad (44)$$

We consider two limiting cases: $L \gg S$ and $S \gg L$. When $L \gg S$, $J \approx L$, so $d\alpha/dt \propto L/r^3 \propto r^{-2.5}$. Equation (8) then implies that $dr/dt \propto r^{-3}$, so $d\alpha/dr \propto r^{1/2}$. Since here we are only interested in the change in α , we set $\alpha = 0$ when $r = 0$. Then $\alpha(r) \propto r^{3/2}$, or $\alpha(f) \propto f^{-1}$, where f is the frequency of the emitted gravity waves at orbital separation r . Thus, of all the precessions that occur in the “observable” frequency range 10–1000 Hz, 90% of them occur in the range 10–100 Hz. That is, most of the precessions occur at *low* frequencies. When $S \gg L$, $J \approx S$, so $d\alpha/dt \propto S/r^3$. Hence $d\alpha/dr$ is constant, so $\alpha(r) \propto r$ and $\alpha(f) \propto f^{-2/3}$. Thus, when $S \gg L$, roughly 80% of the precessions in the observable frequency range occur between 10 and 100 Hz. Typical cases of simple precession will be intermediate between these two limiting cases, so we can expect 80–90% of the “observable” precessions to occur in the 10–100Hz frequency range.

Putting back the constant factors that we omitted in the above scaling analysis, we find

$$\frac{\alpha(f)}{2\pi} \approx \begin{cases} 11 \left(1 + \frac{3M_1}{4M_2} \right) \frac{10M_\odot}{M} \frac{10 \text{ Hz}}{f} & \text{for } L \gg S, \\ 1.9 \left(1 + \frac{3M_1}{4M_2} \right) \frac{M_1}{M_2} \frac{S}{M_1^2} \left(\frac{10M_\odot}{M} \frac{10 \text{ Hz}}{f} \right)^{2/3} & \text{for } S \gg L. \end{cases} \quad (45)$$

Note that when $L \gg S$, the number of precessions is independent of S . This is an important point: slowly spinning bodies produce roughly as many precessions as rapidly spinning ones; however the cone of precession is narrow if S is small.

The “simple” precession of \mathbf{L} and \mathbf{S} around a nearly constant $\hat{\mathbf{J}}$, which we have been discussing, can break down and be replaced by *transitional precession* under just one circumstance: If \mathbf{L} and \mathbf{S} initially point in nearly opposite directions and \mathbf{L} is initially longer than \mathbf{S} [as in Fig. 2(b)], then the orbital inspiral will bring the binary into an epoch [time $t \sim t_3$ in Fig. 2(b)] where $\mathbf{L} \simeq -\mathbf{S}$, and hence J and Ω_p are small and the precession rate is

no longer fast compared to the inspiral rate. Before this small- J epoch, \mathbf{L} and \mathbf{S} undergo simple precession around $\hat{\mathbf{J}}$. Then, during the small- J epoch, the precession becomes transitional: the binary loses its “gyroscopic bearings” and tumbles in space, and that tumbling causes \mathbf{J} to swing around to a new direction, and causes \mathbf{L} and \mathbf{S} , locked onto each other, to swing around with \mathbf{J} . Then, after the small- J epoch, \mathbf{L} and \mathbf{S} resume their simple precessional motion, but now around the new \mathbf{J} direction. We shall explore this transitional precession in Subsec. D below; but first, in Subsecs. B and C, we give a quantitative analysis of simple precession and present some concrete examples.

B. Simple precession

In this section we give a quantitative analysis of simple precession. For ease of analysis, we introduce the notation

$$\kappa \equiv \hat{\mathbf{S}} \cdot \hat{\mathbf{L}}, \quad \gamma(t) \equiv S/L(t). \quad (46)$$

The evolution equations (40a,b) imply that κ is a constant of the motion, whereas (40c,d) imply that γ grows with time: $\dot{\gamma} > 0$. Note, however, that because $S_1 \lesssim M_1^2$ and similarly for body 2, $\gamma(t)$ is bounded above by

$$\gamma \lesssim \frac{M_1^2 + M_2^2}{M_1 M_2} \left(\frac{M}{r} \right)^{1/2}. \quad (47)$$

The magnitude and direction of the total angular momentum can be expressed in terms of κ , $\gamma(t)$, $L(t)$, and the directions $\hat{\mathbf{L}}$ and $\hat{\mathbf{S}}$ as

$$J = L \sqrt{1 + 2\kappa\gamma + \gamma^2}, \quad (48a)$$

$$\hat{\mathbf{J}} = \frac{\hat{\mathbf{L}} + \gamma \hat{\mathbf{S}}}{\sqrt{1 + 2\kappa\gamma + \gamma^2}}, \quad (48b)$$

and correspondingly, the precessional angular velocity (42) can be written as

$$\Omega_p = \left(2 + \frac{3M_2}{2M_1} \right) \sqrt{1 + 2\kappa\gamma + \gamma^2} \frac{L}{r^3}. \quad (49)$$

We now solve for the motion of $\hat{\mathbf{J}}$. Differentiating Eq. (48b) and using the simple precessional equations (40c,d), we find

$$\dot{\hat{\mathbf{J}}} = \frac{\dot{\gamma} \left[\hat{\mathbf{S}}(1 + \kappa\gamma) - \hat{\mathbf{L}}(\kappa + \gamma) \right]}{(1 + 2\kappa\gamma + \gamma^2)^{3/2}}. \quad (50)$$

Thus, at any instant, $\hat{\mathbf{J}}$ moves on the unit sphere along the great-circle arc from $\hat{\mathbf{L}}$ towards $\hat{\mathbf{S}}$; see Fig. 3. Because

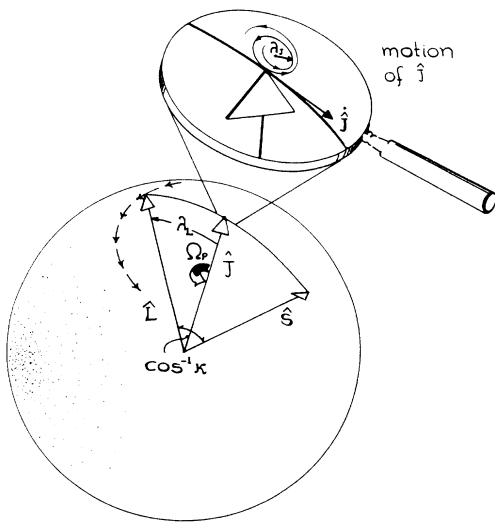


FIG. 3. Simple precession: $\hat{\mathbf{L}}$, $\hat{\mathbf{J}}$, and $\hat{\mathbf{S}}$ undergo tight-spiral motion on the unit sphere, with precessional opening angles $\lambda_J \ll \lambda_L$ and with λ_L gradually increasing; cf. Fig. 2.

$\hat{\mathbf{L}}$ and $\hat{\mathbf{S}}$ are themselves precessing around $\hat{\mathbf{J}}$ with precessional angular velocity Ω_p [Eq. (49)], this (tiny) motion of $\hat{\mathbf{J}}$ must also be a precession at the same angular velocity. We denote by $\hat{\mathbf{J}}_0$ the fixed direction around which $\hat{\mathbf{J}}$ and $\hat{\mathbf{L}}$ both spiral.

The opening angle of the cone on which $\hat{\mathbf{J}}$'s precessional motion takes place is given by

$$\begin{aligned} \lambda_J &= \arcsin \left(\frac{|\dot{\hat{\mathbf{J}}}|}{\Omega_p} \right) = \arcsin \left(\frac{1}{\Omega_p} \frac{\dot{\gamma} \sqrt{1 - \kappa^2}}{(1 + 2\kappa\gamma + \gamma^2)} \right) \\ &= \arcsin \left(\frac{\frac{16}{5} (M/r)^{3/2} \gamma \sqrt{1 - \kappa^2}}{\left(1 + \frac{3}{4} M_1/M_2 \right) (1 + 2\kappa\gamma + \gamma^2)^{3/2}} \right). \end{aligned} \quad (51)$$

Similarly, the opening angle of the cone on which $\hat{\mathbf{L}}$ precesses is

$$\lambda_L = \arcsin \left(\frac{|\dot{\hat{\mathbf{L}}}|}{\Omega_p} \right) = \arcsin \left(\frac{\gamma \sqrt{1 - \kappa^2}}{\sqrt{1 + 2\kappa\gamma + \gamma^2}} \right). \quad (52)$$

Because of the gradual orbital inspiral, the values of the precessional opening angles λ_J and λ_L gradually change; i.e., $\hat{\mathbf{J}}$ and $\hat{\mathbf{L}}$ undergo tight spirals on the unit sphere rather than precise circular motions; see Fig. 3. Because $\lambda_L > 0$ [cf. Fig. 2 or differentiate Eq. (52)], the spiral of λ_L is always outward from $\hat{\mathbf{J}}$. Note that for $\lambda_L < \pi/2$ this means that the cone on which $\hat{\mathbf{L}}$ spirals is opening up around $+\hat{\mathbf{J}}$, but for $\lambda_L > \pi/2$ [as at times $t > t_3$ in Fig. 2(b)], the cone is closing down around $-\hat{\mathbf{J}}$. The tiny spiral of $\hat{\mathbf{J}}$ is outward when $\lambda_L < \pi/2$, and can be either outward or inward when $\lambda_L > \pi/2$, as one can see by differentiating Eq. (51) and comparing with the sign of $\cos \lambda_L = \hat{\mathbf{L}} \cdot \hat{\mathbf{J}} = (1 + \kappa\gamma)/\sqrt{1 + 2\kappa\gamma + \gamma^2}$ [cf. Eq. (48b)].

Note that if $S \gg L$ near the end of the inspiral ($\gamma \gg 1$), then the value of $\cos \lambda_L$ must approach κ at late times, since then $\mathbf{J} \approx \mathbf{S}$. Thus, while $\hat{\mathbf{J}}$ is roughly fixed, $\hat{\mathbf{L}}$ and $\hat{\mathbf{S}}$ effectively “trade places” during the evolution from early to late times: At early times $\hat{\mathbf{L}}$ is close to $\hat{\mathbf{J}}$, and $\hat{\mathbf{S}}$ orbits them at angle $\arccos(\kappa)$ radians away; at late times $\hat{\mathbf{S}}$ and $\hat{\mathbf{J}}$ are close, and $\hat{\mathbf{L}}$ orbits them at an angle $\arccos(\kappa)$ away.

Finally, we show how to put our description of simple precession on a more rigorous basis. In so doing, we will isolate the sufficient condition for simple precession. We described above how the approximate constancy of $\hat{\mathbf{J}}$ arises when the precession timescale Ω_p^{-1} is much shorter than the inspiral timescale L/\dot{L} . Actually, even if the ratio of timescales is small, $\hat{\mathbf{J}}$ can still change significantly in one precession period if the magnitude of \mathbf{J} is much smaller than the magnitude of \mathbf{L} (as can happen if \mathbf{L} and \mathbf{S} are roughly antialigned and have roughly equal magnitude). These considerations suggest defining a “small parameter” $\epsilon = (L/J) \times (\text{ratio of precession timescale to inspiral timescale})$, i.e.,

$$\epsilon \equiv \frac{L \dot{L}/L}{J \Omega_p} = \frac{|\dot{\mathbf{J}}|/J}{\Omega_p}, \quad (53)$$

and solving the precession equations as an expansion in powers of ϵ .

First we note that ϵ is indeed small for “typical” cases. From Eqs. (42) and (8), we have

$$\epsilon = \frac{16}{5} \frac{(M/r)^{3/2}}{\left(1 + \frac{3}{4}M_2/M_1\right)\left(1 + 2\kappa\gamma + \gamma^2\right)}. \quad (54)$$

Thus, for example, $\kappa > 0 \Rightarrow \epsilon < \frac{16}{5}(M/r)^{3/2}$, which is $\ll 1$ except near final coalescence.

We can now justify our assertion that, for small ϵ , both $\hat{\mathbf{J}}$ and $\hat{\mathbf{L}}$ spiral around a single fixed direction, $\hat{\mathbf{J}}_0$. We do so by explicitly exhibiting $\dot{\hat{\mathbf{J}}}_0$:

$$\dot{\hat{\mathbf{J}}}_0 = \hat{\mathbf{J}} - \epsilon \hat{\mathbf{J}} \times \hat{\mathbf{L}}. \quad (55)$$

It is straightforward to check that $\dot{\hat{\mathbf{J}}}_0$ vanishes up to terms of order ϵ^2 . Equivalently, we may write

$$\hat{\mathbf{J}} = \hat{\mathbf{J}}_0 + \epsilon \hat{\mathbf{J}}_0 \times \hat{\mathbf{L}} + O(\epsilon^2). \quad (56)$$

To the same order, $\dot{\hat{\mathbf{L}}}$ is given by

$$\dot{\hat{\mathbf{L}}} = \Omega_p \hat{\mathbf{J}}_0 \times \hat{\mathbf{L}} + \epsilon \Omega_p (\hat{\mathbf{J}}_0 \times \hat{\mathbf{L}}) \times \hat{\mathbf{L}}, \quad (57)$$

where the precession frequency Ω_p is given by Eq. (49).

Finally, dividing Eq. (51) by Eq. (52), we find that

$$\frac{\sin \lambda_J}{\sin \lambda_L} = \epsilon. \quad (58)$$

Thus ϵ being small implies that $\sin \lambda_J$ is small compared to $\sin \lambda_L$, as well as being small compared to unity.

1. Algebraic solution to simple-precession equations

We now solve Eq. (57); this will provide us with an algebraic expression for $\hat{\mathbf{L}}(t)$ which is accurate up to terms of $O(\epsilon^2)$. Referring to Fig. 4, let $\hat{\mathbf{J}}_0$ point in the (θ', ϕ') direction relative to the detector’s Cartesian coordinates (cf. Fig. 1); let α be the instantaneous angular location of $\hat{\mathbf{L}}$ in its precessional motion around $\hat{\mathbf{J}}_0$ with $\alpha = 0$ when

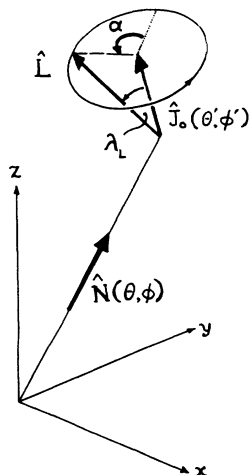


FIG. 4. Geometry for a binary’s simple precession relative to the Earth-based detector’s Cartesian axes; cf. Fig. 1.

$\hat{\mathbf{L}} \cdot \hat{\mathbf{z}}$ is maximum; and note that, by virtue of Eq. (56), the opening angle λ_L of the cone on which $\hat{\mathbf{L}}$ precesses can be regarded equally well as the angle between $\hat{\mathbf{L}}$ and $\hat{\mathbf{J}}_0$, or between $\hat{\mathbf{L}}$ and $\hat{\mathbf{J}}$, aside from fractional errors of order ϵ^2 . Then the geometry of Fig. 4 dictates that

$$\begin{aligned} \hat{\mathbf{L}} = \hat{\mathbf{J}}_0 \cos \lambda_L + \frac{(\hat{\mathbf{z}} - \hat{\mathbf{J}}_0 \cos \theta')}{\sin \theta'} \sin \lambda_L \cos \alpha \\ + \frac{\hat{\mathbf{J}}_0 \times \hat{\mathbf{z}}}{\sin \theta'} \sin \lambda_L \sin \alpha. \end{aligned} \quad (59)$$

Of the quantities appearing in this equation, only λ_L and α change with time during simple precession. By Eq. (48b), $\cos \lambda_L = \hat{\mathbf{L}} \cdot \hat{\mathbf{J}}$ is given by

$$\cos \lambda_L(t) = \frac{\mu \sqrt{Mr(t)} + S_{||}}{\left\{ [\mu \sqrt{Mr(t)} + S_{||}]^2 + S_{\perp}^2 \right\}^{1/2}}. \quad (60)$$

Here $S_{||} \equiv S\kappa$ is the component of the spin \mathbf{S} along $\hat{\mathbf{L}}$, $S_{\perp} = S\sqrt{1 - \kappa^2}$ is the length of its perpendicular component, and $r(t)$ is given by Eq. (8). A similar algebraic expression for the angular position α of $\hat{\mathbf{L}}$ can be obtained from its differential equation:

$$d\alpha/dt = \Omega_p(t) \quad (61)$$

[Eq. (57) dotted into $\hat{\mathbf{J}}_0 \times \hat{\mathbf{L}}$]. Changing the independent variable from t to r using (8), Eq. (61) becomes

$$\frac{d\alpha}{dr} = \frac{-5}{32} \left(\frac{1 + \frac{3}{4}M_2/M_1}{\mu M^2} \right) \left[(\mu \sqrt{Mr} + S_{||})^2 + S_{\perp}^2 \right]^{1/2}. \quad (62)$$

This is easily integrated to give

$$\begin{aligned} \alpha = \frac{-5(1 + \frac{3M_2}{4M_1})}{96\mu^3 M^3} & \left[2Y^{3/2} - 3S_{||}(\mu \sqrt{Mr} + S_{||})\sqrt{Y} \right. \\ & \left. - 3S_{||}S_{\perp}^2 \operatorname{arcsinh} \left(\frac{\mu \sqrt{Mr} + S_{||}}{S_{\perp}} \right) \right] + \text{const}, \end{aligned} \quad (63a)$$

where

$$Y \equiv \mu^2 Mr + 2S_{||}\mu\sqrt{Mr} + S^2. \quad (63b)$$

This completes our solution for $\hat{\mathbf{L}}(t)$ for our two special cases. As a check, we have integrated the orbital evolution equations (40) numerically for a broad range of initial conditions and have found that, whenever the constraint $\epsilon \ll 1$ is satisfied, the evolution is in excellent accord with the “simple”-precession behavior embodied in Eqs. (56), (59), (60), and (63).

2. Algebraic expressions for simple-precession waveforms

The gravitational waveforms emitted by the binary are described by Eqs. (18)–(21), and (10), (29), and (4), in

$$\hat{\mathbf{L}} \cdot \hat{\mathbf{N}} = \hat{\mathbf{J}}_0 \cdot \hat{\mathbf{N}} \left[\cos \lambda_L - \frac{\cos \theta' \sin \lambda_L \cos \alpha}{\sin \theta'} \right] + \frac{\cos \theta \sin \lambda_L \cos \alpha}{\sin \theta'} + \hat{\mathbf{N}} \cdot (\hat{\mathbf{J}}_0 \times \hat{\mathbf{z}}) \frac{\sin \lambda_L \cos \alpha}{\sin \theta'}, \quad (64a)$$

$$\hat{\mathbf{N}} \cdot (\hat{\mathbf{L}} \times \hat{\mathbf{z}}) = \hat{\mathbf{N}} \cdot (\hat{\mathbf{J}}_0 \times \hat{\mathbf{z}}) \left[\cos \lambda_L - \frac{\cos \theta' \sin \lambda_L \cos \alpha}{\sin \theta'} \right] + (\hat{\mathbf{N}} \cdot \hat{\mathbf{z}} \cos \theta' - \hat{\mathbf{N}} \cdot \hat{\mathbf{J}}_0) \frac{\sin \lambda_L \sin \alpha}{\sin \theta'}, \quad (64b)$$

$$\hat{\mathbf{L}} \cdot \hat{\mathbf{z}} = \cos \theta' \cos \lambda_L + \sin \theta' \sin \lambda_L \cos \alpha, \quad (64c)$$

where

$$\hat{\mathbf{J}}_0 \cdot \hat{\mathbf{N}} = \cos \theta \cos \theta' + \sin \theta \sin \theta' \cos(\phi - \phi'), \quad (64d)$$

$$\hat{\mathbf{N}} \cdot (\hat{\mathbf{J}}_0 \times \hat{\mathbf{z}}) = \sin \theta \sin \theta' \sin(\phi - \phi'), \quad (64e)$$

and λ_L and α are given by Eqs. (60) and (63). This completes the solution for $h_+(t)$, $h_\times(t)$, $A(t)$, and $\varphi(t)$.

As was noted following Eq. (29), $\delta\Phi(t)$ cannot be expressed as a function of $\hat{\mathbf{N}}$ and the instantaneous value of $\hat{\mathbf{L}}$; it depends on the full time history of $\hat{\mathbf{L}}$ between

$$\int_0^{2\pi} \frac{d\delta\Phi}{d\alpha} d\alpha = \begin{cases} -2\pi \cos \lambda_L & |\hat{\mathbf{J}}_0 \cdot \hat{\mathbf{L}}| < |\hat{\mathbf{J}}_0 \cdot \hat{\mathbf{N}}|, \\ 2\pi(-\cos \lambda_L + 1) & \hat{\mathbf{J}}_0 \cdot \hat{\mathbf{L}} > |\hat{\mathbf{J}}_0 \cdot \hat{\mathbf{N}}|, \\ 2\pi(-\cos \lambda_L - 1) & \hat{\mathbf{J}}_0 \cdot \hat{\mathbf{L}} < -|\hat{\mathbf{J}}_0 \cdot \hat{\mathbf{N}}|. \end{cases} \quad (65)$$

We see from Eq. (65) that the “average value” of $\delta\Phi$ can be roughly as large as the precessional frequency Ω_p . Thus the term “ $2\delta\Phi$ ” in Eqs. (18) can change the total number of cycles in the wave fields and the observed waveform by roughly twice the total number of precessions—a sizable correction.

This completes our analytic treatment of simple precessional waveforms for our two special cases.

C. Examples of simple precession

1. $1M_\odot$ neutron star and maximally spinning $10M_\odot$ black hole

As an example of simple precession and the waveform modulation it produces, consider a $M_2 = 1M_\odot$ nonspinning neutron star spiraling into a $M_1 = 10M_\odot$ maximally rotating black hole, so $S = S_1 = M_1^2$. (We also gave a brief discussion of this example in Ref. [3].) We shall begin following the binary’s evolution at an initial moment $t_c - t_i = 204$ s before the final collision when the orbital radius is $r_i = 63.2M$ and the gravitational-wave frequency (twice the orbital frequency) is $f_i = 11.7$ Hz. This is roughly the time when the gravity wave signal enters the frequency band accessible to the advanced LIGO/VIRGO detectors. We shall follow the

which $h_+(t)$, $h_\times(t)$, $A(t)$ and $\varphi(t)$ are represented as simple algebraic functions of $\hat{\mathbf{L}}(t)$, and $\delta\Phi$ is represented as an integral of a simple algebraic function of $\hat{\mathbf{L}}(t)$. In these formulae, $\hat{\mathbf{L}}(t)$ appears in the combinations $\hat{\mathbf{L}} \cdot \hat{\mathbf{N}}$, $\hat{\mathbf{N}} \cdot (\hat{\mathbf{L}} \times \hat{\mathbf{z}})$ and $\hat{\mathbf{L}} \cdot \hat{\mathbf{z}}$. Straightforward algebra based on Eq. (59) gives for these quantities

$$\hat{\mathbf{L}} \cdot \hat{\mathbf{N}} = \hat{\mathbf{J}}_0 \cdot \hat{\mathbf{N}} \left[\cos \lambda_L - \frac{\cos \theta' \sin \lambda_L \cos \alpha}{\sin \theta'} \right] + \frac{\cos \theta \sin \lambda_L \cos \alpha}{\sin \theta'} + \hat{\mathbf{N}} \cdot (\hat{\mathbf{J}}_0 \times \hat{\mathbf{z}}) \frac{\sin \lambda_L \cos \alpha}{\sin \theta'}, \quad (64a)$$

$$\hat{\mathbf{N}} \cdot (\hat{\mathbf{L}} \times \hat{\mathbf{z}}) = \hat{\mathbf{N}} \cdot (\hat{\mathbf{J}}_0 \times \hat{\mathbf{z}}) \left[\cos \lambda_L - \frac{\cos \theta' \sin \lambda_L \cos \alpha}{\sin \theta'} \right] + (\hat{\mathbf{N}} \cdot \hat{\mathbf{z}} \cos \theta' - \hat{\mathbf{N}} \cdot \hat{\mathbf{J}}_0) \frac{\sin \lambda_L \sin \alpha}{\sin \theta'}, \quad (64b)$$

$$\hat{\mathbf{L}} \cdot \hat{\mathbf{z}} = \cos \theta' \cos \lambda_L + \sin \theta' \sin \lambda_L \cos \alpha, \quad (64c)$$

time t and the end point of coalescence, t_c . However, the growth of this phase shift over one precession period can be described by an approximate analytical expression. That expression turns out to depend on whether the line containing $\hat{\mathbf{N}}$ lies outside or inside $\hat{\mathbf{L}}$ ’s cone of precession (i.e., on whether $|\hat{\mathbf{J}}_0 \cdot \hat{\mathbf{N}}|$ is greater or less than $|\hat{\mathbf{J}}_0 \cdot \hat{\mathbf{L}}|$), but is otherwise independent of $\hat{\mathbf{N}}$. If we approximate $\cos \lambda_L$ as constant over one precession period, then by changing variables from t to α using $d\alpha/dt = \Omega_p$, we find (with some effort) that

evolution up to $t_c - t_f = 0.03$ s, when the orbital radius is $r_f = 6.96M$ and the gravitational-wave frequency is $f_f = 321$ Hz. Because photon shot noise in the broad band detectors rises sharply for $f > 100$ Hz, more than 99% of the signal-to-noise has been accumulated by this point. Note that as the binary spirals in from r_i to r_f , the parameter $\gamma = S/L$ increases from $\gamma_i = 1.258$ to $\gamma_f = 3.79$. Thus, throughout the LIGO/VIRGO observational band, the hole’s spin angular momentum is somewhat larger than the orbital angular momentum.

In our example the orbit has a modest inclination to the hole’s equatorial plane, $\arccos(\hat{\mathbf{L}} \cdot \hat{\mathbf{S}}) = 11.3^\circ$ (0.197 radians), so $\kappa = \hat{\mathbf{L}} \cdot \hat{\mathbf{S}} = 0.9806$. Then, as the binary spirals in from $r_i = 63.2M$ to $r_f = 6.96M$, the opening angle of $\hat{\mathbf{L}}$ ’s precession cone increases from $\lambda_{L,i} = 6.30^\circ$ to $\lambda_{L,f} = 8.95^\circ$, and the parameter $\epsilon = \sin \lambda_J / \sin \lambda_L$ that characterizes our simple-precession approximation increases from $\epsilon_i = 1.17 \times 10^{-3}$ to $\epsilon_f = 7.11 \times 10^{-3}$. With ϵ so small, our approximation is excellent throughout the inspiral.

In our example, the binary is directly underfoot as seen from the detector, so $\hat{\mathbf{N}} = -\hat{\mathbf{z}} + \delta\hat{\mathbf{x}}$, where δ is an arbitrarily small angle [required because some of our formulas, e.g., Eq. (5), become singular for sources that are precisely overhead or underfoot]. At the initial time t_i , the orbit is precisely edge-on as seen from Earth, with the orbital plane parallel to the detector’s $\hat{\mathbf{x}}$ arm

and the orbital angular momentum along its \hat{y} arm, so $\hat{L}_i = \hat{y}$; and the black hole's spin is parallel to the detector's plane (perpendicular to our line of sight), so $\hat{S}_i = 0.9806\hat{y} - 0.1960\hat{x}$. These initial conditions are depicted in the upper left portion of Fig. 5. The subsequent precessional motion of \hat{L} is shown in Fig. 6. The initial position of \hat{L} in this figure is at the origin (since $\hat{L}_i = \hat{y}$), which corresponds to an angular location $\alpha_i = \pi/2$ in the conventions of the previous subsection. The total number of precessions during the inspiral from $r_i = 63.2M$ to $r_f = 6.96M$ is $(\alpha_f - \alpha_i)/2\pi = 23.8$. The opening up of the precession cone from $\lambda_{Li} = 6.30^\circ$ to $\lambda_{Lf} = 8.95^\circ$ is evident in the figure. The center of the precession cone is at $\hat{J}_0 = \hat{J} = -0.1097\hat{x} + 0.9940\hat{y}$ (aside from fractional corrections of order ϵ).

The gravitational-wave signals from this binary are depicted in Figs. 5 and 7, for two possible orientations of the detector. The first orientation, referred to as $+$ in Figs. 5 and 7, is the one assumed until now in all of this paper's formulas and figures: arms along \hat{x} and \hat{y} , so $h(t) = \frac{1}{2}(h_{xx}^{\text{TT}} - h_{yy}^{\text{TT}}) \equiv h_{+}$ (where h_{jk}^{TT} is the

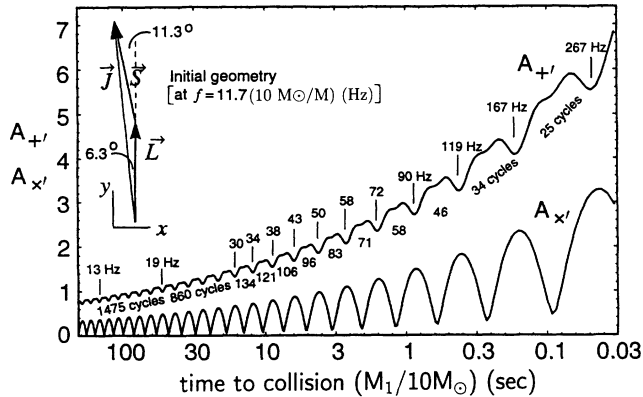


FIG. 5. Amplitude modulation of the gravitational-wave signals from a nonspinning $M_2 = 1M_\odot$ neutron star spiraling into a maximally spinning $M_1 = 10M_\odot$ black hole. The binary is underfoot as seen from the detector of Fig. 1, with its initial spin, orbital, and total angular momenta as shown in the upper left part of this figure (where the direction \hat{N} from Earth to the binary is into the paper). The $+$ detector, whose measured wave amplitude A_+ is shown here as a function of time $t_c - t$ to final collision, has arms oriented along the \hat{x} and \hat{y} directions (as in Fig. 1), i.e. along the horizontal and vertical axes of the upper left part of this figure. The x' detector, with measured wave amplitude $A_{x'}$, has its arms rotated 45° to the $+$ detector, i.e., along $\frac{1}{2}(\hat{x} + \hat{y})$ and $\frac{1}{2}(-\hat{x} + \hat{y})$. The signals' amplitude A and phase φ (Fig. 7) are defined by Eq. (6), where $\Phi(t)$ is the angular position of the binary in its orbit; cf. Fig. 1. The vertical scale in this figure is arbitrary, but linear. This figure (and the accompanying Figs. 6, 7, and 8) are also correct for any other binary with the same geometry, same mass ratio $M_2/M_1 = 0.1$, same $S_2 = 0$ and same maximal spin $S_1/M_1^2 \equiv 1$, but different M_1 ; the only change is an increase in the time scale by a factor $M_1/10M_\odot$ and a decrease in all frequencies by the inverse factor $10M_\odot/M_1$. Setting $M_1 = 10^5M_\odot$ gives an example relevant to proposed space-based interferometers; see Sec. IV C 2.

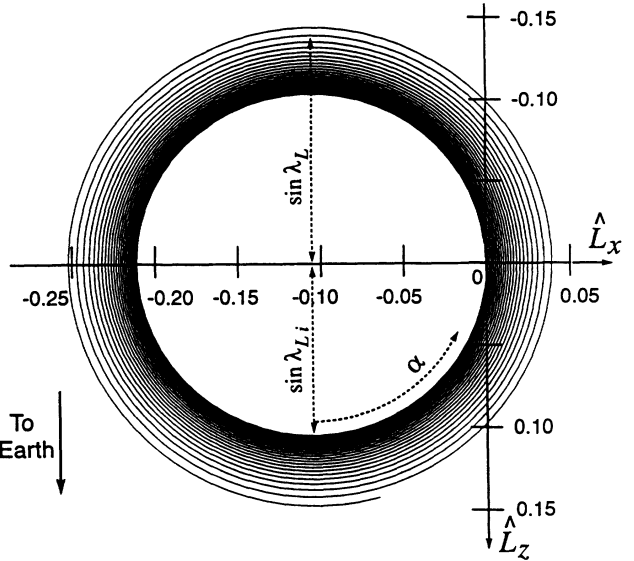


FIG. 6. The precession of \hat{L} (and hence also of the orbital plane) for the binary whose initial conditions are depicted in the upper left part of Fig. 5.

"transverse-traceless," tensorial gravitational-wave field [14]). The second orientation, referred to as x' in the figures, is rotated 45° relative to the first, so the arms are along $\frac{1}{2}(\hat{x} + \hat{y})$ and $\frac{1}{2}(-\hat{x} + \hat{y})$, and $h(t) = h_{xy}^{\text{TT}} \equiv h_{x'}$.

The amplitudes $A_{+}(t)$ and $A_{x'}(t)$ of the signals $h(t)$ measured by these two detectors are shown in Fig. 5. Each complete period of the orbit's precession produces one cycle of amplitude modulation; the 23.8 precessions in the LIGO band produce 23.8 modulation periods.

Along the $A_{+}(t)$ curve is marked the gravitational waves' carrier frequency $f = \Omega/\pi$. Because the radiation reaction grows stronger as the binary spirals inward, the carrier frequency sweeps upward ("chirps") at a gradually growing rate. Also indicated along the $A_{+}(t)$ curve is the number of carrier-frequency oscillation cycles

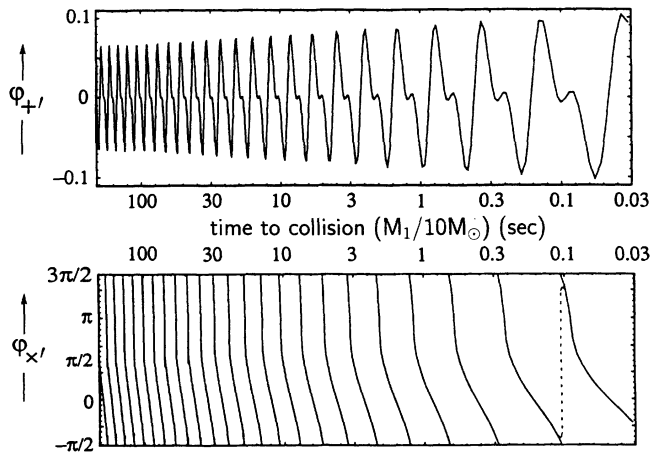


FIG. 7. Polarization phase of the gravitational-wave signals for the binary and detectors of Fig. 5. The phases φ_{+} and $\varphi_{x'}$ are shown, modulo 2π , as functions of time to collision $t_c - t$.

during one (or, early on, several) modulation periods. Early in the LIGO/VIRGO band there are several hundred carrier cycles per modulation cycle; late, there are several tens. The modulation shapes are explained in the Appendix using diagrammatic tools developed there to provide an intuitive understanding of precession-induced modulation.

The fundamental modulation frequency [which is equal to the binary's precession frequency $\Omega_p/2\pi \sim (1/\pi)J/r^3$] remains finite in the limit that \mathbf{S} and \mathbf{L} are parallel. By contrast, the depth ΔA of the modulation goes to zero in the limit of parallel \mathbf{S} and \mathbf{L} , because the opening angle λ_L of the orbit's precession cone goes to zero.

Since in our example the precession cone is rather narrow, $\lambda_L \simeq 0.1$ rad, it should not be surprising that the modulation depth is modest for the $+$ -oriented detector: $\Delta A_{+}/A_{+} \simeq \lambda_L \simeq 0.1$. Remarkably, by contrast, for the \times' detector, the modulation is very large: $\Delta A_{\times'}/A_{\times'} \simeq 1$. The reason is that once each cycle, the precession carries the binary near a special orientation $\hat{\mathbf{L}} \simeq \hat{\mathbf{y}}$, which is half-way between the \times' detector's two arms; by symmetry, the \times' detector's response vanishes for this orientation. One might have expected that, because of the narrowness of the precession cone, the binary would always be near this \times' -suppressing orientation, and therefore $A_{\times'}$ would remain always $\lesssim \lambda_L A_{+} \simeq 0.1 A_{+}$. Not so. Each cycle of precession carries $\hat{\mathbf{L}}$ through an angle of $\Delta\psi \simeq 2\lambda_L \simeq 0.2$ rad in the detector plane; and this drives the signal amplitude up to $A_{\times'} \simeq \sin(2\Delta\psi)A_{+} \simeq 4\lambda_L A_{+} \simeq 0.4 A_{+}$. This explains how, despite the narrow precession cone, the \times' signal manages to have *both* a relatively large maximum amplitude $A_{\times' \text{ max}} \simeq \frac{1}{2} A_{+}$, and a very large depth of modulation, $\Delta A_{\times'} \simeq A_{\times'}$.

Our example also illustrates a general *rule of thumb for simple precession*: The maximum amplitude A_{max} of a detector's signal during a modulation cycle is generally in the range $(0\text{--}1)A_{+ \text{ max}}$, where $A_{+ \text{ max}}$ is the maximum amplitude of the principal+ mode during the precession; and the depth ΔA of the modulation is generally in the range $(0\text{--}1)\sin(4\lambda_L)A_{+ \text{ max}}$ (but of course $\Delta A \leq A$).

Figure 7 shows the polarization phases $\varphi_{+}(t)$ and $\varphi_{\times'}(t)$ for the two detectors. For the $+$ detector, the modulation of the polarization phase is modest: $\Delta\varphi_{+} \sim 0.1$ to 0.2 rad. For the \times' detector, the polarization phase modulation is very large: $\varphi_{\times'}$ grows secularly, though at a somewhat irregular rate, changing by -2π with each cycle of orbital precession. As is discussed in detail in the appendix, this secular growth of $\varphi_{\times'}(t)$ is caused by the fact that each precession takes $\hat{\mathbf{L}}$ once around $\hat{\mathbf{y}}$, the bisector of the detector's two arms (see Fig. 6). If the binary's orientation were shifted away from $\hat{\mathbf{y}}$ (leftward in Fig. 6) by an additional 3° , then $\hat{\mathbf{L}}$ would still pass near the arms' bisector $\hat{\mathbf{y}}$ during each precession but would not go around it; as a result, the polarization phase would have the finite-oscillation form that is shown as a dotted line in Fig. 7. Although the solid and dotted curves look radically different, the effects on the signal $h(t)$ are only slightly different for the two cases: the signal is not sensitive to 2π changes in φ ; and modulo 2π , the solid and dotted $\varphi_{\times'}(t)$ are essentially

identical, except for the very short time when the dotted curve is flying upward.

Finally, Fig. 8 shows the phase correction term $2\delta\Phi$ throughout the inspiral. (We recall that this term is independent of the waves' polarization and independent of detector orientation, and that by convention it vanishes at the end of the inspiral.) In this example, $2\delta\Phi$ accumulates slowly because $\hat{\mathbf{N}}$ does not lie inside $\hat{\mathbf{L}}$'s precession cone and $\cos\lambda_L$ is close to 1; cf. Eq. (65). Moreover the accumulation is very steady, since $\hat{\mathbf{L}}$ never comes close to $\hat{\mathbf{N}}$.

2. $10^4 M_\odot/10^5 M_\odot$ black-hole binary

Because the equations of orbital dynamics and waveform generation do not contain any intrinsic, binary-independent length scale, the solutions are easily scaled from one binary to another binary with the same values of all dimensionless quantities, but different absolute masses and spins. For example, Figs. 6–8 remain valid if we increase the mass M_1 of the black hole by some arbitrary factor and increase all times and decrease all frequencies by that same factor, while holding fixed the dimensionless quantities $M_2/M_1 = 0.1$, $S_2 = 0$, $S_1/M_1^2 = 1$, $\hat{\mathbf{L}} \cdot \hat{\mathbf{S}} = \kappa = 0.9806$, and the keeping initial orientations as shown in the upper left of Fig. 5.

Most interestingly, if we increase M_1 by a factor 10^4 , we obtain an example relevant to space-based interferometric detectors such as the proposed LISA mission [13]. The binary is made of a nonspinning $10^4 M_\odot$ black hole and a maximally spinning $10^5 M_\odot$ black hole; instead of sweeping upward through the LIGO/VIRGO band from $f_i = 11.7$ Hz to $f_f = 321$ Hz, the waves depicted in the figures sweep through the band of space-based interferometers, from $f_i = 0.00117$ Hz to 0.0321 Hz; and instead of lasting for $t_c - t_i = 204$ s, the depicted waves last for 2.04×10^6 s or about a month, which is a reasonable measurement time for a space-based interferometer. (On the other hand, it is not at all obvious whether the event rate for $\sim 10^4 M_\odot/10^5 M_\odot$ black-hole-black-hole binaries will be interesting, even given that the proposed detectors could see them out to cosmological distances.)

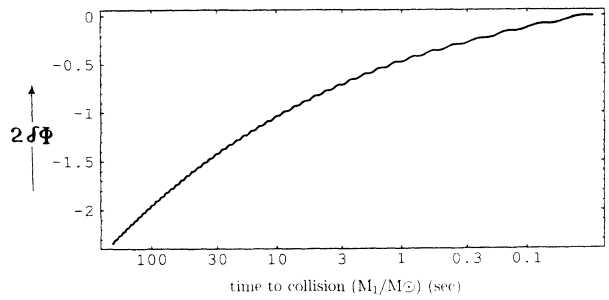


FIG. 8. The phase correction term $2\delta\Phi$ for the binary of Fig. 5, shown as a function of time to collision $t_c - t$. This term is independent of detector orientation.

3. Neutron-star–neutron-star binaries

When the binary's two bodies have equal masses, $M_1 = M_2$, their orbital angular momentum $L = \mu\sqrt{Mr} = \frac{1}{4}M^2\sqrt{r/M}$ is always somewhat larger than their maximum possible total spin, $S_{\max} \simeq M_1^2 + M_2^2 = \frac{1}{2}M^2$. As a result, the total angular momentum \mathbf{J} is always fairly close to \mathbf{L} , which means that the opening angle λ_L of the precession cone is always small.

For example, consider two equal mass neutron stars, $M_1 = M_2 = 1.4M_\odot$, each with maximal spin, and with $\hat{\mathbf{S}}$ inclined at the same angle to $\hat{\mathbf{L}}$ as in our previous $M_1/M_2 = 10$ examples: $\arccos(\hat{\mathbf{S}} \cdot \hat{\mathbf{L}}) = 11.3^\circ$. Then, as the waves' carrier frequency sweeps through our previously chosen band of 11.7 Hz to 321 Hz, the precession cone grows from $\lambda_L \simeq 1.5^\circ$ to 3.6° . With precession so tight, the modulation is typically quite weak: For the initial spin, orbit, and detectors oriented as in our previous Fig. 5, the '+' detector has amplitude and phase modulations shaped very much like those of Figs. 5 and 7, but with modulation amplitudes $\Delta A_{+}/A_{+} \sim \Delta\varphi_{+} \sim 0.01$. As before, the very specially oriented 'x' detector shows deep modulation like that in Figs. 5 and 7, but only at a price of having an amplitude roughly 10 times smaller than that of the '+' detector: $A_{x'}/A_{+} \sim 4\lambda_L \sim 1/10$.

As another example, let one of the $1.4M_\odot$ neutron stars be maximally spinning ($S_1 = M_1^2$) and the other be non-spinning ($S_2 = 0$), and open up the angle between $\hat{\mathbf{S}}$ and $\hat{\mathbf{L}}$ to 60° (so $\kappa = \hat{\mathbf{L}} \cdot \hat{\mathbf{S}} = 0.5$). For variety, change the initial geometry to that shown in Fig. 11 (which is presented in another context in Sec. V A): The detector's arms are along the $\hat{\mathbf{x}}$ and $\hat{\mathbf{y}}$ axis (as in all our formulae); the binary instead of being underfoot is at a zenith angle of 45° along the same azimuth as the $\hat{\mathbf{x}}$ arm, i.e., $\hat{\mathbf{N}} = (\hat{\mathbf{z}} - \hat{\mathbf{x}})/\sqrt{2}$; the total angular momentum (and hence the center of the precession cone) points directly upward, $\hat{\mathbf{J}} = \hat{\mathbf{z}}$; and $\hat{\mathbf{L}}$ and $\hat{\mathbf{S}}$ initially are oriented around $\hat{\mathbf{J}}$ as shown. The resulting amplitude modulation of the detector's signal is shown in Fig. 11 below (where in the horizontal frequency scale we must set $M = 2.8M_\odot$). Although the modulation is modest, growing from roughly 15% to roughly 30% during the inspiral, the number of precessions is rather large: Between 10 Hz and 1000 Hz there are 70 precession periods, with 90% of them occurring between 10 Hz and 100 Hz [in good agreement with Eq. (45)].

D. Transitional precession

1. General description

In this section we discuss transitional precession. Our understanding of this behavior is based largely on numerical integrations of our special-case precession equations (40) for $S_2 = 0$ or $M_1 = M_2$. We have not been able to derive an approximate analytic solution for $\hat{\mathbf{L}}(t)$ during transitional precession, as we could for simple precession, but the main qualitative features of the phenomenon are clear.

Since $L \propto r^{1/2}$ while S is constant during the inspiral, at sufficiently early times L is always much larger than S , $\mathbf{J} \approx \mathbf{L}$, $\epsilon \ll 1$, and the binary undergoes simple precession. However, if $\hat{\mathbf{L}}$ and $\hat{\mathbf{S}}$ are nearly antialigned, and if $S > L$ by the end of the inspiral, then the binary must pass through an intermediate stage when \mathbf{L} and \mathbf{S} almost cancel and hence J is much smaller than L or S . In this intermediate stage, $\epsilon \equiv \dot{L}/(J\Omega_p) = |\dot{\mathbf{J}}|/(J\Omega_p)$ is large ($\gtrsim 1$) for two reasons: L/J is large and $\Omega_p^{-1} \propto r^3/J$ is large. Now, recall that the “simplicity” of simple precession was due to the smallness of the parameter ϵ . The simple precessional motion that we described in Sec. IV B therefore breaks down, and (in numerical examples) $\hat{\mathbf{L}}$ and $\hat{\mathbf{S}}$ appear to “tumble,” while locked in each others’ embrace. The tumbling continues until the orbit has shrunk to the point that L is significantly smaller than S . At that point $J \approx S$, and simple precession resumes. Because the tumbling stage represents a short-lived “transition” between two stages of simple precession, we call it *transitional precession*.

In the initial stage of simple precession, $\hat{\mathbf{J}}$ moves on a tight outward spiral away from some initial direction $\hat{\mathbf{J}}_i = (\hat{\mathbf{J}}_0)_{\text{initial}}$, while $\hat{\mathbf{L}}$ (which is approximately equal to $\hat{\mathbf{J}}$) moves on a looser outward spiral away from $\hat{\mathbf{J}}_i$. During transitional precession, $\hat{\mathbf{J}}$ “migrates” from the vicinity of $\hat{\mathbf{J}}_i$ towards a new, fixed location $\hat{\mathbf{J}}_f = (\hat{\mathbf{J}}_0)_{\text{final}}$. In the final stage of simple precession, $\hat{\mathbf{J}}$ moves on a tight, inward spiral towards $\hat{\mathbf{J}}_f$, while $\hat{\mathbf{L}}$ points almost 180° away from $\hat{\mathbf{J}}$ and spirals more loosely inwards towards $-\hat{\mathbf{J}}_f$.

Figure 9 illustrates the evolution of $\hat{\mathbf{L}}(t)$ before, during, and after transitional precession. In the example shown, $M_1/M_2 = 10$, $S_1 = M_1^2$, $S_2 = 0$, $\cos^{-1}\kappa = 179.3^\circ$, and the epoch of evolution shown begins when $r = 330M$ and $f = 1(10M_\odot/M_1)$ Hz, and ends when $r = 6M$ and $f = 400(10M_\odot/M_1)$ Hz.

The entire sequence that we have just described—from simple to transitional and then back to simple precession—will typically *not* take place during the time that the binary is “visible” to LIGO/VIRGO (or, in the

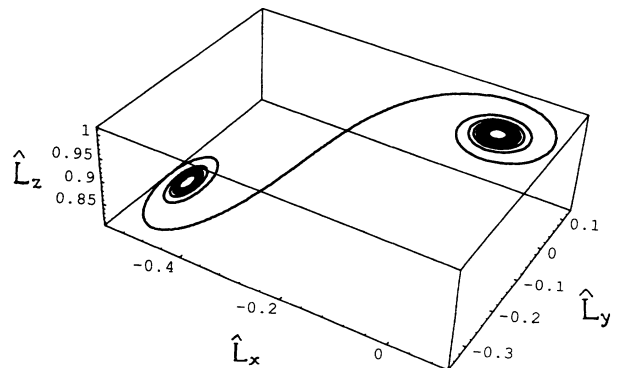


FIG. 9. An example of the path traced by $\hat{\mathbf{L}}(t)$ during the evolution from simple precession to transitional precession and back to simple precession. In this example, $M_1/M_2 = 10$, $\arccos(\kappa) = 179.3^\circ$, r/M decreases from ~ 330 to 6 , and f increases from $1(10M_\odot/M_1)$ Hz to $400(10M_\odot/M_1)$ Hz.

supermassive-binary case, to LISA). It is easy to see why: To include the entire sequence, the binary must enter the observational band with $L/S \gtrsim 2$ and leave it with $L/S \lesssim 2$, which means that L must change by a factor 4 or more in the observational band. Since $f \propto r^{-3/2} \propto L^{-3}$, this means that f must change by $\gtrsim 4^3 = 64$. However, $f_{\max}/f_{\min} \sim 64$ is the entire available observational band for both LIGO/VIRGO (with $f_{\min} \sim 10$ Hz and $f_{\max} \sim 500$ Hz) and LISA (with $f_{\min} \sim 10^{-3}$ Hz and $f_{\max} \sim 10^{-1}$ Hz). Therefore, to include the entire sequence, one must carefully adjust M_1 , M_2 , S_1 , and $\kappa = \hat{\mathbf{S}} \cdot \hat{\mathbf{L}}$ so the spin and orbital angular momenta are nearly antialigned, and so $L/S \simeq 2$ when the binary is just entering the observational band, and $L/S \simeq 1/2$ when it is just leaving. Moreover, one must choose M_1/M_2 large enough that, when the binary begins its final coalescence (at $r/M \sim 6$), L/S has gotten at least as small as $1/2$.

Just how precisely antialigned must $\hat{\mathbf{L}}$ and $\hat{\mathbf{S}}$ be, i.e., how close to -1 must $\kappa \equiv \hat{\mathbf{L}} \cdot \hat{\mathbf{S}}$ be, to produce transitional precession? It is clear from the previous discussion that transitional precession occurs when ϵ becomes of order unity. Let us define

$$\delta \equiv \kappa + 1. \quad (66)$$

Using Eq. (54) we find that, for small δ , ϵ reaches its maximum value when $\gamma = (1 + 2\delta)$, which corresponds to an orbital separation $r_{\max}/M = (S/M_1 M_2)^2(1 - 4\delta)$; there ϵ is

$$\epsilon_{\max} \approx \frac{8}{5} \delta^{-1} \left(1 + \frac{3M_2}{4M_1} \right)^{-1} \left(\frac{M}{r_{\max}} \right)^{3/2} \quad (67)$$

for small δ . [Equation (67) assumes that ϵ does in fact reach a maximum at some finite r .] Thus, for transitional precession to occur ($\epsilon \gtrsim 1/2$) at $r_{\max}/M \gtrsim 20$ (when there is still a significant number of orbits to go before the binary's final coalescence), δ must be $\lesssim 0.04$ so $\kappa = -1 + \delta$ must lie between -1.0 and -0.96 , which means that the angle between $\hat{\mathbf{L}}$ and $\hat{\mathbf{S}}$ must exceed 164° . Thus, we see that transitional precession will be observed for only a very narrow range of initial conditions.

Even if $\hat{\mathbf{L}}$ and $\hat{\mathbf{S}}$ are sufficiently antialigned to produce transitional precession, the rest of the fine tuning will typically not be achieved in nature. Either L/S will be somewhat less than 2 when the binary enters the observational band, and the initial period of simple precession will be lost in the detector's low-frequency noise; or else L/S will be somewhat greater than $1/2$ when the binary leaves the observational band, and the final period of simple precession will be lost in the detector's high-frequency noise, or will not occur at all because orbital plunge and final coalescence intervene.

2. Remarks on the final direction of $\hat{\mathbf{J}}$

When the full sequence of simple precession to transitional precession to simple precession occurs, how does the final direction of the binary's total angular momentum, $\hat{\mathbf{J}}_f = (\hat{\mathbf{J}}_0)_{\text{final}}$, depend on its initial direction,

$\hat{\mathbf{J}}_i = (\hat{\mathbf{J}}_0)_{\text{initial}}$, and on the binary's masses and spins? We do not have a complete answer to this question, but it is perhaps useful to include here some general remarks and an example. (In this discussion, we ignore the possibility that the inspiral ends before $S \gg L$.)

For this discussion, it is convenient to introduce spherical coordinates (θ', ϕ') on the unit sphere, with $\hat{\mathbf{J}}_i$ at the north pole, $\theta' = 0$. We choose the location of the meridian $\phi' = 0$ as follows. We choose some instant of time which is defined in a dimensionless way, such as the moment when $r/M = 100$ or the moment when $L = S$, and we let $\phi' = 0$ correspond to the direction of $\hat{\mathbf{J}}$ at that instant. It is then clear by the scale invariance of the problem that the coordinates of $\hat{\mathbf{J}}_f$ can depend *only* on the following dimensionless quantities: κ , M_2/M_1 , and S/M^2 .

We obtain qualitative information about the dependence of $\hat{\mathbf{J}}_f$ on these quantities by considering two limiting cases. First consider the case where κ is precisely -1 . Then $\hat{\mathbf{J}}$ simply "flips" when L becomes smaller than S , so $\hat{\mathbf{J}}_f = -\hat{\mathbf{J}}_i$. The second, obvious limiting case is that $\hat{\mathbf{J}}_f \rightarrow \hat{\mathbf{J}}_i$ for $\kappa \gg -1$.

By continuity, we see that $\hat{\mathbf{J}}_f$ must move from $\theta' = \pi$ to $\theta' = 0$ as we increase κ away from -1 . Because typically all this motion occurs as κ changes by only ~ 0.04 , $\hat{\mathbf{J}}_f$ must be a rather sensitive function of κ .

Figure 10 shows the path traced out by $\hat{\mathbf{J}}_f$ as the angle $\arccos(\kappa)$ between $\hat{\mathbf{L}}$ and $\hat{\mathbf{S}}$ is varied, for one particular choice of mass and spin ratios: $M_2/M_1 = 0.2$, $S = S_1 = M_1^2$, and $S_2 = 0$. Each point on the curve is the end result of evolving the precession equations (40) from very early to very late times to determine $\hat{\mathbf{J}}_f$. In each evolution, $\hat{\mathbf{J}}_i$ was taken to be at $\theta' = 0$, and $\phi' = 0$

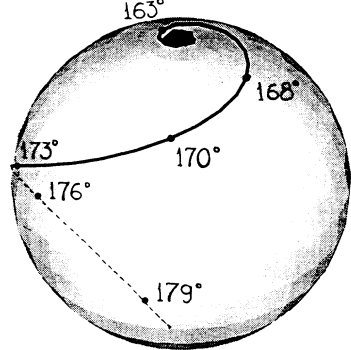


FIG. 10. The end point of transitional precession, i.e., the direction $\hat{\mathbf{J}}_f$ of the binary's total angular momentum $\hat{\mathbf{J}}$ at asymptotically late times, expressed as a function of the initial direction $\hat{\mathbf{J}}_i$ of $\hat{\mathbf{J}}$ (which is taken to be the north pole, $\theta' = 0$) and of the angle $\arccos(\kappa)$ between $\hat{\mathbf{L}}$ and $\hat{\mathbf{S}}$. The mass and spin ratios are chosen to be $M_2/M_1 = 0.2$, $S_1/M_1^2 = 1$, and $S_2 = 0$. Each point on the curve is the result of evolving the precession equations (40) from early to late times for that point's value of κ . One more piece of initial data, besides $\hat{\mathbf{J}}_i$, is needed to fully specify the evolution: the azimuthal direction of $\hat{\mathbf{J}}$ at some early, but finite, time. In this figure, $\hat{\mathbf{J}}$ is chosen to point in the direction $\phi' = 0$ at the moment when the gravity wave frequency f equals $10(M/10M_\odot)$ Hz.

was defined by the location of $\hat{\mathbf{J}}$ at the moment that the gravity wave frequency f swept through $10(M/10M_\odot)$ Hz. For the chosen mass and spin ratios, $r_{\max}/M \approx 25$, so from Eq. (67) we would expect transitional precession to “turn off” ($\epsilon \lesssim 1/2$) for $\kappa \gtrsim -0.978$, when the angle between $\hat{\mathbf{L}}$ and $\hat{\mathbf{S}}$ is roughly 168° . This is in reasonable agreement with the numerical results shown in Fig. 10.

V. NUMERICAL SOLUTIONS FOR ARBITRARY MASSES AND SPINS

A. Relation of the general case to our special cases

In this section we move beyond our two special cases, $M_1 = M_2$ and $S_2 = 0$, and discuss binaries with arbitrary masses and spins (consistent with the requirement that $S_i \leq M_i^2$). In this general case we were unable to solve the precession equations (11) analytically, and so had to resort to numerical integrations. One would expect, however, that, for “typical” inspirals, the precessional behavior will qualitatively resemble the simple precession described in Sec. IV, if precession is important to the dynamics at all. That expectation is based on the following argument, which begins by dividing binaries into two categories based on their mass ratio: $M_2/M_1 \ll 1$ and $M_2/M_1 \approx 1$. If $M_2/M_1 \ll 1$, the amplitude of precession will be very small unless $S_1 \gg S_2$, since $S_2/L(t) \leq (M_2/M_1)[M/r(t)]^{1/2} \ll 1$. If $S_1 \gg S_2$, the larger spin should dominate the precessional dynamics, and the smaller spin can be treated as a perturbation on the special-case solutions of Sec. IV. Similarly, if $M_1 \approx M_2$, the mass difference can be treated as a perturbation to our special case solutions for $M_1 = M_2$.

The above argument is not very compelling, especially when applied to “intermediate” cases such as $M_2/M_1 = 1/2$. One therefore seeks guidance from numerically generated examples. Now, in principle one could systematically look for qualitatively new types of solutions by integrating the precession equations (11) for thousands of randomly chosen values of M_1 , M_2 , S_1 , S_2 , and initial directions $\hat{\mathbf{S}}_1$ and $\hat{\mathbf{S}}_2$. This we have not attempted to do. However, we have integrated equations (11) for a wide variety of initial conditions which we “put in by hand”; the results seem to support the conclusion that most cases give “somewhat ragged” versions of the simple precession described in Sec. IV B. That is, $\hat{\mathbf{J}}$ is roughly fixed, and $\hat{\mathbf{L}}(t)$ roughly traces an outward spiral from $\hat{\mathbf{J}}$.

To illustrate this, Figs. 11–18 display several examples of numerical solutions to the precession equations (11), augmented by the signal-amplitude equations (19a) and (20). The drawing in each figure depicts the initial values of the vectors \mathbf{L} , \mathbf{S}_1 , \mathbf{S}_2 , and \mathbf{S} at the moment that the gravity wave frequency sweeps past $10(10M_\odot/M)$ Hz (corresponding to $r/M = 75$). For ease of comparison, we have chosen $\mathbf{J} = \mathbf{S} + \mathbf{L}$ to point initially along the $\hat{\mathbf{z}}$ -axis in all our examples; the precise details of how the other initial vectors were chosen are spelled out in the caption of Fig. 11. In each figure, the curve on the sphere is the time evolution of $\hat{\mathbf{L}}(t)$ from the initial mo-

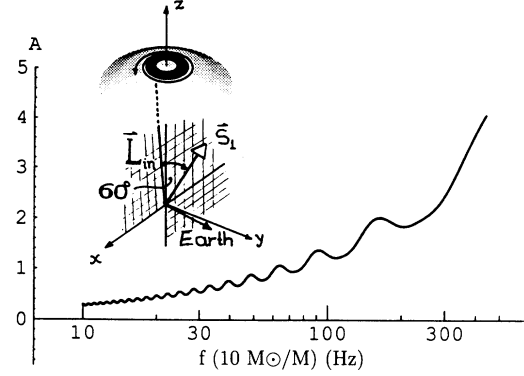


FIG. 11. This and the next seven figures (Figs. 11–18) depict the precession of the orbital angular momentum direction $\hat{\mathbf{L}}$ and the resulting modulated signal amplitude $A(t)$ in the detector, as computed by numerical integrations of the precession equations (11) together with Eqs. (19a) and (20). In all these figures the detector's legs are along the x and y axes, the direction from the detector to the binary is $\hat{\mathbf{N}} = (\hat{\mathbf{z}} + \hat{\mathbf{x}})/\sqrt{2}$, the total spin $\mathbf{S} = \mathbf{S}_1 + \mathbf{S}_2$ has magnitude $S = M_1^2$, the angle between the orbital angular momentum \mathbf{L} and the total spin \mathbf{S} is 60° so $\kappa = \hat{\mathbf{L}} \cdot \hat{\mathbf{S}} = 0.5$ (except in Figs. 17 and 18, where that angle is 178° and $\kappa = -0.99939$), and at the beginning of the integration—when $f = 10(10M_\odot/M)$ Hz, $r/M = 75$, and $L = \sqrt{75}M_1M_2$ —the total angular momentum $\mathbf{J} = \mathbf{L} + \mathbf{S}$ points in the z direction, and $\hat{\mathbf{L}}$ is in the x - z plane, on the $+x$ side of the z -axis, while $\hat{\mathbf{S}}$ is in the x - z plane, on the $-x$ side of the z -axis. When both bodies are spinning (Figs. 12, 14, 16, and 18), their spins initially lie in the $\hat{\mathbf{y}}\text{-}\hat{\mathbf{S}}$ plane. The figures differ from each other in their mass ratio M_2/M_1 and in the magnitudes of the bodies' spins. In this figure, the masses are equal, $M_2/M_1 = 1$, body 1 is maximally spinning, $S_1 = M_1^2$, and body 2 is nonspinning, $S_2 = 0$, so $\mathbf{S} = \mathbf{S}_1$ and \mathbf{L} have the initial values shown in the drawing. The subsequent motion of $\hat{\mathbf{L}}$ is shown as an outward-spiraling path on the sphere. The graph shows the amplitude $A(t)$ of the gravitational-wave signal measured by the detector.

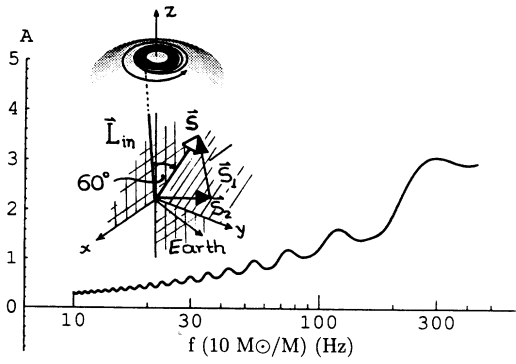


FIG. 12. Same as Fig. 11, and with the same mass ratio $M_1/M_2 = 1$ but with both bodies maximally spinning, $S_1 = M_1^2$, $S_2 = M_2^2$, so the initial \mathbf{S}_1 , \mathbf{S}_2 , \mathbf{S} , and \mathbf{L} are as shown.

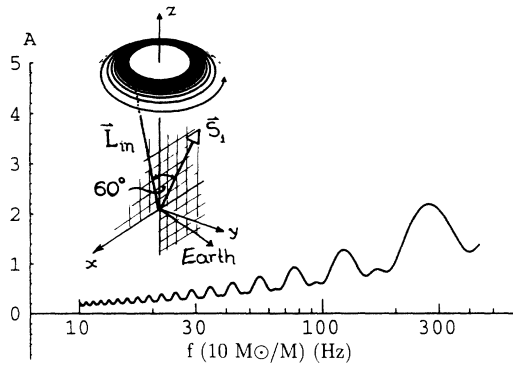


FIG. 13. Same as Fig. 11, but with $M_2/M_1 = 0.3$, $S_1 = M_1^2$ and $S_2 = 0$, so the initial \mathbf{S}_1 and \mathbf{L} are as shown.

ment, when $f = 10(10M_\odot/M)$ Hz and $r/M = 75$ to a final moment, when $f = 440(10M_\odot/M)$ Hz and $r/M = 6$. The curve plotted in each figure is the amplitude $A(t)$ of the gravity-wave signal that would be measured by a detector whose arms lie along the \hat{x} and \hat{y} axes, when the binary is in the direction $\hat{\mathbf{N}} = (\hat{\mathbf{z}} + \hat{\mathbf{x}})/\sqrt{2}$. The signal amplitude $A(t)$ is actually plotted against the frequency f of the gravity wave signal at time t ; that is, we plot $A(f) \equiv A(t(f))$. [We emphasize that we are *not* plotting the Fourier transform of $A(t)$.] The overall normalization of $A(f)$ is arbitrary.

We have arranged Figs. 11–18 in pairs: an example with just one body spinning, $S_1 = M_1^2$ and $S_2 = 0$ (for which the special-case theory of Sec. IV is valid), is paired with a corresponding example having the same mass ratio and same initial \mathbf{L} and \mathbf{S} , but with both bodies maximally spinning, so $S_1 = M_1^2$ and $S_2 = M_2^2$. We emphasize that when both bodies are spinning (Figs. 12, 14, 16, and 18) the precession and signal amplitude depicted are solutions of the full post²-Newtonian precession equations (11), *including the spin-spin terms*; the spin-spin terms either vanished identically or were ignored in our analysis of special cases in Sec. IV.

The first pair of examples, Figs. 11 and 12, are for a mass ratio $M_2/M_1 = 1.0$ and for $\kappa = 0.5$ (so the angle between $\hat{\mathbf{L}}$ and $\hat{\mathbf{S}}$ is 60°). Because the two masses are equal,

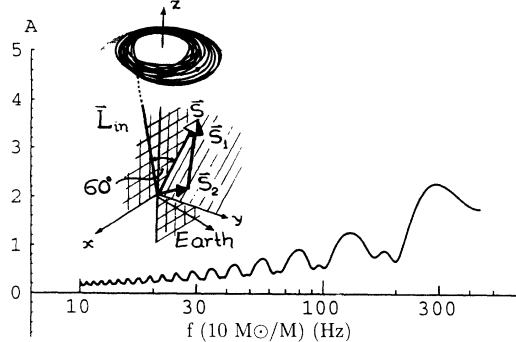


FIG. 14. Same as Fig. 11, but with $M_2/M_1 = 0.3$ (as in Fig. 13) and $S_1 = M_1^2$, $S_2 = M_2^2$, so the initial \mathbf{S}_1 , \mathbf{S}_2 , \mathbf{S} , and $\hat{\mathbf{L}}$ are as shown.

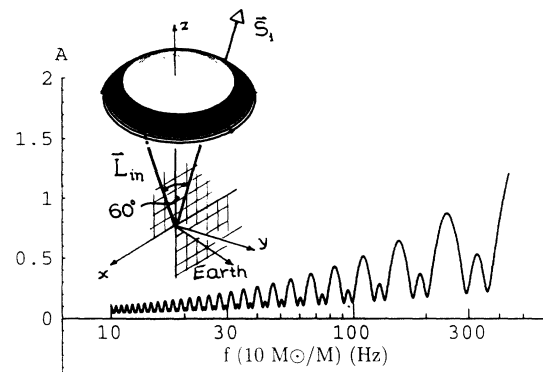


FIG. 15. Same as in Fig. 11, but with $M_2/M_1 = 0.1$, $S_1 = M_1^2$ and $S_2 = 0$, so the initial \mathbf{S}_1 and \mathbf{L} are as shown.

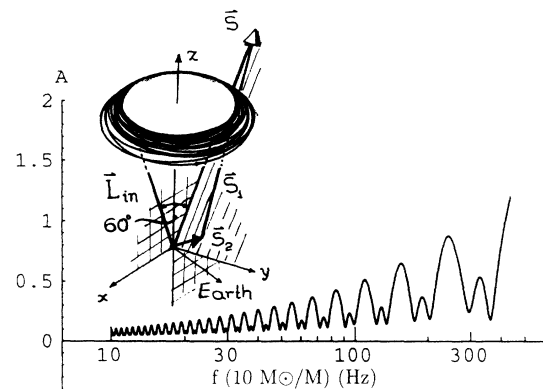


FIG. 16. Same as in Fig. 11, but with $M_2/M_1 = 0.1$ (as in Fig. 15) and $S_1 = M_1^2$, $S_2 = M_2^2$, so the initial \mathbf{S}_1 , \mathbf{S}_2 , \mathbf{S} , and $\hat{\mathbf{L}}$ are as shown.

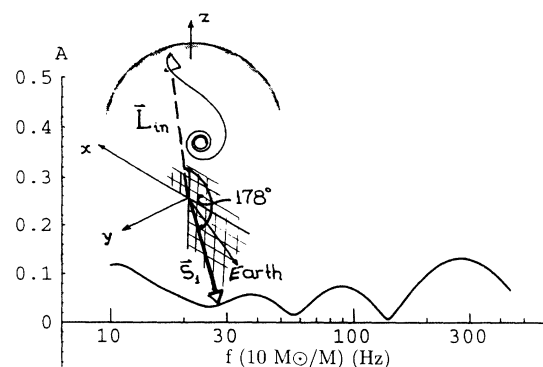


FIG. 17. Same as in Fig. 11, but with $\hat{\mathbf{L}}$ and $\hat{\mathbf{S}}$ nearly antialigned (i.e., separated by an angle of 178° so $\kappa = -0.99939$), and with $M_2/M_1 = 0.13$, $S_1 = M_1^2$, and $S_2 = 0$, so the initial \mathbf{S}_1 and \mathbf{L} are as shown. The evolution illustrates transitional precession and the subsequent return to simple precession.

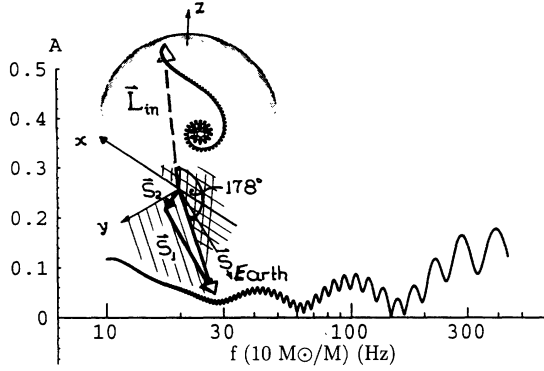


FIG. 18. Same as in Fig. 11, but with the same near antialignment and mass ratio as in Fig. 17 (angle 178° between $\hat{\mathbf{L}}$ and $\hat{\mathbf{S}}$, $\kappa = -0.99939$, $M_2/M_1 = 0.13$), and with $S_1 = M_1^2$, $S_2 = M_2^2$, so the initial \mathbf{S}_1 , \mathbf{S}_2 , \mathbf{S} , and \mathbf{L} are as shown. The evolution is essentially the same as in Fig. 17, but with visible “epicycles” due to the relatively rapid precession of \mathbf{S}_2 around \mathbf{L} .

the solutions for $\hat{\mathbf{L}}(t)$ and $A(t)$ shown in Figs. 11 and 12 would be identical, were it not for the spin-spin terms in Eqs. (11). We see that the spin-spin effects are noticeable, but do not change the basic, qualitative behavior of the solution. Quantitatively, the $S_2 = 0$ case contains 0.5 fewer precessions in the observable range than the case where S_2 is maximal.

Figures 13 and 14 show an example where $M_2/M_1 = 0.3$ and $\kappa = 0.5$; while Figs. 15 and 16 are for $M_2/M_1 = 0.1$ and $\kappa = 0.5$. Again, the precessional motion of \mathbf{L} and the signal amplitude are nearly the same in the corresponding cases, i.e., the effect of the second spin is small. This is to be expected, since $S_2/S_1 = M_2^2/M_1^2$ is 0.09 in Fig. 14 and 0.01 in Fig. 16.

Finally, in Figs. 17 and 18 we show an example containing transitional precession. Here $M_2/M_1 = 0.13$ and $\kappa = -0.99939$ (so the angle between $\hat{\mathbf{L}}$ and $\hat{\mathbf{S}}$ is 178°), and our integrations start [at $f = 10(10M_\odot/M)$ Hz] when the transitional precession is already underway: the figures show the end of transitional precession and the resumption of simple precession. The two solutions for $\hat{\mathbf{L}}(t)$ are again qualitatively similar, but, interestingly, the two-spin case (Fig. 18) displays a large number of “epicycles” on top of the basic one-spin evolution (Fig. 17). The epicycles are reflected in the many little wiggles visible in the waveform’s amplitude.

We can understand these epicycles as follows: Since $S_2/S_1 = (0.13)^2 = 0.017$, we can treat the second spin as a perturbation. Actually, the formulation is slightly simpler if we treat $M_2/M_1 = 0.13$ as the expansion parameter rather than S_2/S_1 , while regarding M_1 and S_2/M_2^2 as fixed. Then \mathbf{S}_2 is second order in the expansion parameter, and \mathbf{S}_2 is first order. [The term \mathbf{S}_2 is of higher order than $\hat{\mathbf{S}}_2$ because the epicyclic frequency diverges as $M_2 \rightarrow 0$; see Eq. (11c).] We define $\mathbf{L}(t) \equiv \mathbf{L}_1(t) + \mathbf{L}_2(t)$, where $\mathbf{L}_1(t)$ is the “background” solution and $\mathbf{L}_2(t)$ represents the perturbation in $\mathbf{L}(t)$ due to \mathbf{S}_2 . The term $\mathbf{L}_2(t)$ is second order, and $\hat{\mathbf{L}}_2(t)$ is first order. We now expand the precession equations (11) to first order. Adding

Eqs. (11a) and (11b), we find

$$\dot{\mathbf{L}}_2 + \dot{\mathbf{S}}_2 = 0. \quad (68)$$

We can absorb the constant of integration into the definition of \mathbf{L}_1 ; this leaves $\mathbf{L}_2 = -\mathbf{S}_2$. The first-order piece of Eq. (11c) then becomes

$$\dot{\mathbf{L}}_2 = \left(\frac{1}{r^3} \right) \left(\frac{3M_1}{2M_2} \right) \mathbf{L}_1 \times \mathbf{S}_2. \quad (69)$$

We see from Eq. (69) that \mathbf{L}_2 spirals around \mathbf{L}_1 with an epicyclic frequency

$$\Omega_e = (3M_1/2M_2) L/r^3 \quad (70)$$

that is larger than the precession frequency Ω_p by a factor $(3M_1/4M_2)L/J$. Using Eq. (8) for dr/dt , the total number of epicycles between some large radius r and the final plunge can be estimated to be $\sim (1/80)(M_1/M_2)(r/M)^{3/2}$. This corresponds to ~ 60 epicycles for the case shown in Fig. 18, in good agreement with the numerical integration.

Since basically this same perturbation analysis can be applied to the situations shown in Figs. 14 and 16, one might wonder why epicycles are not visible in those figures. The reason is that in these cases the ratio of epicyclic frequency to precession frequency is much closer to unity than is the case in Fig. 18, and also the ratio $|\mathbf{S}_2 \times \mathbf{L}|$ to $|\mathbf{S}_1 \times \mathbf{L}|$ is much smaller. Therefore it is harder to pick out the epicycles by eye.

In conclusion, it appears that the intuitive pictures that we have derived from the study of special cases in Sec. IV can be successfully applied to more general values of the mass and spin parameters. The “extra wiggles” that arise in the general case can be understood as perturbations on our special case solutions.

ACKNOWLEDGMENTS

We thank Eanna Flanagan for helpful conversations. The orbital-precession and wave-generation aspects of this research were supported in part by NSF Grant AST-9114925 and, in view of its application to proposed detectors in space, by NASA Grant NAGW-2897. The application to ground-based gravitational-wave detection was supported in part by NSF Grant PHY-9213508. The last several months of Cutler’s contribution to this work were supported by Grant AST-9119475 at Cornell University.

APPENDIX: FOUNDATIONS FOR AN INTUITIVE UNDERSTANDING OF THE WAVEFORM MODULATION

In leading order (when one ignores orbital inspiral, precession, and post-Newtonian effects), the gravitational waves from a circular binary are monochromatic, and therefore have elliptical polarization. (We regard circular and linear polarizations as special cases of elliptical.) In this appendix we develop a set of diagrammatic tools (Figs. 19, 20, 21, and 23) for describing such waves and

the signals they produce in a detector. These diagrammatic tools are especially useful when the waves come from overhead or underfoot, i.e., when the plane of the detector is orthogonal to the waves' propagation direction. For obliquely inclined detectors, one must apply the tools to each detector arm separately, and then combine the signals.

In Secs. 1 and 2 of the Appendix, we diagrammatically describe the waves alone (without any detector); the culmination of this description is an *elliptical polarization diagram*, which is simply related to the elliptical projection of the binary's orbital plane on the sky. In Sec. 3 we show, by examples, how to use this polarization diagram (or, equivalently the orbit's elliptical projection) to deduce the precession-induced modulations of the signal in a detector. In Sec. 4 we derive some formulas that underlie another diagrammatic tool, the *cell diagram*, by which one can deduce especially simply the signal's polarization phase φ . In Sec. 5 we present the cell diagram and show how to use it. Sections 3, 4, and 5 are restricted to detectors orthogonal to the propagation direction. In Sec. 6 we comment on the application of our techniques to obliquely inclined detectors.

1. Elliptically polarized gravitational waves

In building our diagrammatic tools, we shall focus initially on an arbitrary, monochromatic, elliptically polarized gravitational wave. Only later, in Sec. 2, will we apply these tools to the waves from a circular binary.

For monochromatic waves, the dimensionless gravitational wave fields h_+ and h_\times , as they pass through the laboratory, are given by

$$h_+ = H_+ \cos(\omega t), \quad h_\times = \pm H_\times \sin(\omega t). \quad (\text{A1})$$

Here the + sign corresponds to right-hand polarized waves and the - sign to left-hand; H_+ and H_\times are constants, the amplitudes of the two polarization states, and we have omitted an arbitrary phase by our choice of the zero of time. By convention we shall insist that both amplitudes be positive and that $H_+ \geq H_\times$. The waves will take the form (A1), with its phase delay of precisely $\pm\pi/2$ radians between the two wave fields and with $H_+ > H_\times$, only for a special, unique choice of the polarization axes with respect to which the "+" and "×" states are defined. We shall call that unique choice the elliptical waves' *principal axes*. Figure 19 shows an example of principal axes for waves that are propagating perpendicularly out of the paper. [To verify that any other ("primed") choice of axes will produce a non $\pm\pi/2$ phase shift between the two fields, one need only insert Eq. (A1) into the following standard expression [14] for the primed-axis fields in terms of the principal-axis fields

$$h_{+'} + ih_{\times'} = (h_+ + ih_\times)e^{-2i\psi} \quad (\text{A2})$$

and evaluate the resulting phases of $h_{+’}$ and $h_{\times’}$. In Eq. (A2), ψ is the angle of rotation to go from the principal axes to the primed axes.]

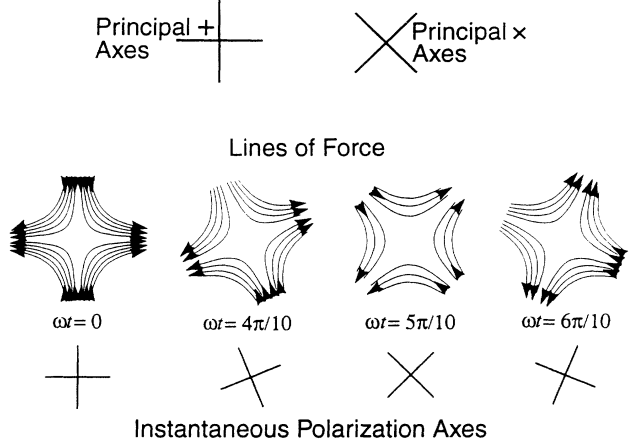


FIG. 19. Principal axes, instantaneous lines of force, and instantaneous polarization axes for an elliptically polarized gravitational wave with right-hand polarization and amplitude ratio $H_\times/H_+ = 0.5$.

The instantaneous tidal accelerations exerted on matter by any gravitational wave can be described by electrical-like "lines of force"; see, e.g., Ref. [14]. Figure 19 shows the evolution of these lines of force for the monochromatic, right-hand elliptical waves of Eq. (A1), with $H_\times/H_+ = 0.5$.

Note that the lines of force rotate in a right-hand manner (recall that the waves are propagating out of the paper), and as they rotate, the density of force lines oscillates. Just as in electromagnetic theory, so also here, the density of force lines is proportional to the magnitude of the wave-induced accelerations. The accelerations are strongest at $\omega t = 0$, when only the "principal+" polarization is active, and weakest at $\omega t = \pi/2$ when only the "principal×" polarization is active. Note that the rotation of the force lines is very nonuniform: slow near $\omega t = 0$ when the large principal+ mode is active, and fast near $\omega t = \pi/2$ when the small principal× mode is active.

Figure 20(a) is a simpler way of depicting the rota-

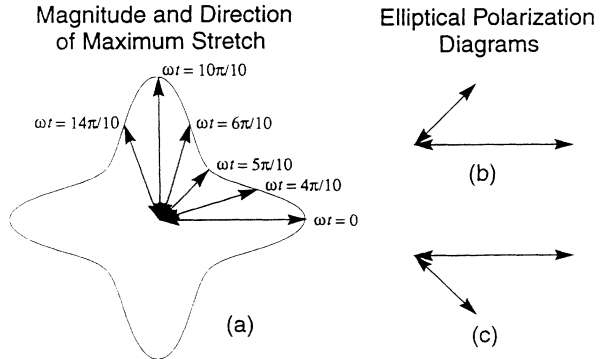


FIG. 20. (a) The rotating, oscillating stretch line which depicts the direction and magnitude of maximum tidal stretch for the gravitational waves of Fig. 1. (b) The elliptical polarization diagram for these same waves. (c) The polarization diagram for these waves but with their handedness changed from right to left.

tion and oscillation of the instantaneous force lines. Here we are asked to remember that the shapes of the force lines are quadrupolar; and at each moment of time we show, via a double-arrowed line, the direction of the instantaneous tidal stretch axis (the direction of maximum tidal stretch), and the magnitude of the tidal acceleration along that axis. As time passes, the stretch axis rotates and the magnitude of the acceleration oscillates (big horizontal stretch at $\omega t = 0$, small 45° stretch at $\omega t = \pi/2$, big vertical stretch at $\omega t = \pi$, etc.).

Figure 20(b) (which we shall call an *elliptical polarization diagram* or simply *polarization diagram*) embodies the same information as Fig. 20(a), but more simply. It shows just two tidal stretch lines, the long one at $\omega t = 0$, which points along a principal+ stretch axis and has length proportional to H_+ ; and the shorter one at $\omega t = \pi/2$, which points along the principal \times axis and has length proportional to H_\times . From this diagram, one can reconstruct both the rotating, oscillating stretch line of Fig. 20(a) and the time-evolving force lines of Fig. 19. To do so, one just needs to remember that (i) the quadrupolar-shaped lines of force rotate from the longer stretch line toward the shorter one, (ii) the magnitude of the tidal accelerations is maximum when one of the instantaneous polarization axes coincides with the longer stretch line and then it is proportional to the stretch line's length, and similarly (iii) the magnitude of the accelerations is minimum when an instantaneous polarization axis coincides with the shorter stretch line and then it is proportional to that stretch line's length.

Figure 20(c) is a polarization diagram for the same waves as we have been discussing, but with left-hand polarization rather than right: the lines of force rotate clockwise from the long stretch line toward the short one, rather than counterclockwise as in Fig. 20(b).

2. Specialization to waves from circular binaries

Turn, now, to the leading-order gravitational waves from a circular binary (with inspiral, precession, and post-Newtonian effects ignored). Figure 21(a) depicts the orbit of one of the binary's stars (or black holes), projected onto the plane of the Earth's sky (i.e., pro-

jected perpendicular to the incoming waves' propagation direction). Because of the projection, the circular orbit looks elliptical, with a ratio α of minor axis to major axis given by

$$\alpha \equiv |\hat{\mathbf{L}} \cdot \hat{\mathbf{N}}|. \quad (\text{A3})$$

In Sec. II we defined the *principal+ direction* to be the major axis of this orbital ellipse, and the *principal \times direction* to be rotated 45° from it, in a counterclockwise direction. The binary emits elliptically polarized waves toward Earth. The waves' principal+ axes coincide with the major and minor axes of the projected orbital ellipse as shown in Fig. 21(b), i.e., one principal+ axis is along the principal+ direction and the other is perpendicular to it; and similarly for principal \times . With respect to these principal+ and principal \times axes, the waves are described by Eq. (A1), with amplitudes [cf. Eq. (2)]

$$H_+ = \frac{4M_1M_2}{rD} \frac{[1 + (\hat{\mathbf{L}} \cdot \hat{\mathbf{N}})^2]}{2}, \quad H_\times = \frac{4M_1M_2}{rD} |\hat{\mathbf{L}} \cdot \hat{\mathbf{N}}|. \quad (\text{A4})$$

Here, as in the body of this paper, M_1 and M_2 are the masses of the two bodies, r is the orbital diameter, and D the distance of the binary from the Earth. The factor $-\hat{\mathbf{L}} \cdot \hat{\mathbf{N}}$ in H_\times guarantees that the waves' handedness is the same as the motion of the stars around their projected orbit (left hand in Fig. 21).

From the wave fields (2), their amplitudes (A4), and the principal+ axes of Fig. 21(b), we infer that the elliptical polarization diagram has the form shown in Fig. 21(c). Notice the very simple relationship of this polarization diagram to the projection of the orbit on the sky: The longer stretch axis is perpendicular to the projected orbit's major axis, i.e., perpendicular to the principal+ direction (as will always be the case); the shorter stretch axis is rotated 45° in the direction of the orbital motion (as will always be the case), i.e., in this case of left-hand polarized waves it is along the principal \times direction while for right-hand waves it would be perpendicular to principal \times ; the length of the shorter stretch is proportional to $\alpha = |\hat{\mathbf{L}} \cdot \hat{\mathbf{N}}|$ (the orbit's axis ratio); and the length of the longer stretch is proportional to $\frac{1}{2}(1 + \alpha^2)$. At a retarded time when the stars' separation is along the principal+ direction [so one of the stars is at the location shown in Fig. 21(c)], the instantaneous *squeeze* axis is along that principal+ direction, i.e., along the direction from the center of the orbit to the star [cf. the minus sign in Eqs. (2) and (6)], and the instantaneous stretch axis is perpendicular to that direction, i.e., along the long stretch line of Fig. 21(c). (It is this that dictates our drawing the long stretch axis perpendicular to the principal+ direction rather than along it.) An eighth of an orbit later, when the star in Fig. 21(c) has moved from the tail to the tip of the thin orbital arrow, the instantaneous squeeze axis is along the direction to that star, and the instantaneous stretch axis is perpendicular to that direction, i.e., along the short stretch line of Fig. 21(c).

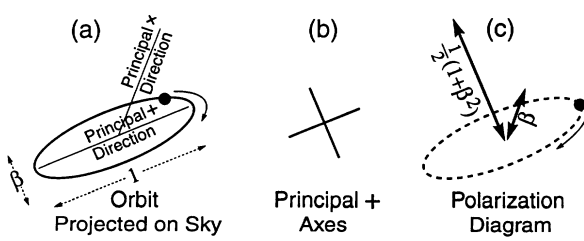


FIG. 21. (a) The orbit of one of the stars in a circularized binary, projected on the plane of the sky. (b) The principal+ axes of the elliptically polarized waves emitted by this binary; note that these axes coincide with the projected orbit's principal axes; the principal \times axes will be rotated 45° to the orbit's axes. (c) The elliptical polarization diagram for the emitted waves.

3. Signal modulation for detectors orthogonal to the waves' propagation direction

Figure 21 provides a simple, intuitive understanding of how a binary's precession modulates its gravitational waves: As the binary precesses, the eccentricity and orientation of its projected orbit [Fig. 21(a)] oscillate, and the polarization diagram [Fig. 21(c)], which describes the waves, oscillates in the obvious, corresponding manner.

It is fairly easy, from the oscillating polarization diagram, to understand the modulation of the amplitude $A(t)$ and polarization phase $\varphi(t)$ of the signal that the wave induces in a detector. As an example, consider the neutron-star-black-hole binary studied in Sec. IV C 1, for which $A(t)$ and $\varphi(t)$ were depicted in Figs. 5 and 7 assuming two different detector orientations, $+$ ' and \times' . Recall that in this example the source is precisely underfoot; i.e., the detector arms are orthogonal to the direction of wave propagation. In this section and the next two, we shall restrict attention to cases where the detector is directly underfoot or overhead.

Figure 22 reproduces a short segment of the amplitudes' time evolution (Fig. 5). In the upper left is a schematic picture of the precessing orbital-angular-momentum direction $\hat{\mathbf{L}}$ (see also Fig. 6). The waves are traveling vertically out of the paper, and the detectors' arms are oriented as indicated by the $+$ ' and \times' symbols. The time-evolving projection of the orbit on the plane of the sky is depicted in the center of the figure. When the orbit is edge-on, we see only a line. When $\hat{\mathbf{L}}$ is tilted away from Earth, we see the orbit from below (shown as a shaded ellipse); the stars move around the ellipse in a clockwise direction, and the waves therefore are left-hand polarized. When $\hat{\mathbf{L}}$ is tilted toward Earth, we see the orbit from above (shown as a white ellipse); the stars move around the ellipse counterclockwise, and the waves are right-hand polarized.

Consider the amplitude A_{+}' measured by the $+$ ' detector, and mentally factor out its steady, overall growth due to the steady orbital inspiral. At time t_a , the orbit is edge on, so the waves are concentrated entirely in the principal $+$ mode; and because the edge-on orbit is almost parallel to one of the $+$ ' detector's arms, that detector feels the full force of the principal $+$ waves. At

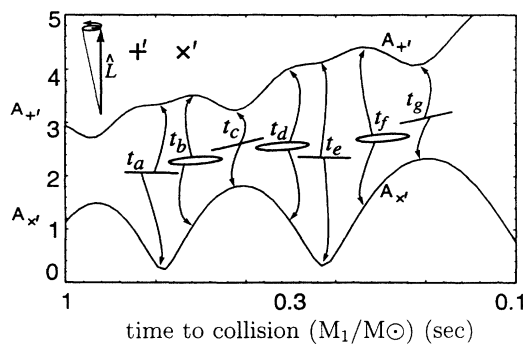


FIG. 22. Figure used to explain the modulation of the signal amplitudes $A_{+}'(t)$ and $A_{\times}'(t)$ for the binary and detectors of Figs. 5, 6, and 7.

time t_b , $\hat{\mathbf{L}}$ has tilted away from Earth a bit, thereby making the orbit appear somewhat elliptical and giving a bit of added strength to the principal $+$ waves. [Recall that their strength H_+ is proportional to $\frac{1}{2}(1 + \alpha^2)$, where α is the ratio of the minor to major axis of the ellipse.] Because the orbit's major axis is still nearly parallel to a detector arm, the detector still "feels" solely the principal $+$ mode (even though H_x is no longer zero), and it feels the mode's full strength; hence, A_{+}' has gone up a bit. At time t_c , the orbit has become edge-on again so H_x is again zero, but now the orbit is tilted away from the detector's arm by $2\lambda_L \simeq 17^\circ$, thereby reducing somewhat the $+$ ' detector's response to the principal $+$ mode; as a result, A_{+}' has decreased significantly. At time t_d , the orbit is tilted toward Earth and has thus become somewhat elliptical once again, thereby enhancing H_+ ; and again the orbit is nearly parallel to the detector's arm, so the detector feels nearly the full force of the principal $+$ mode. As a result, A_{+}' has gone up again. At time t_e , the orbit's major axis is still nearly parallel to the detector arm. Hence the detector still feels nearly the full force of the principal $+$ mode, but the orbit is now edge-on, so H_+ has been reduced, and A_{+}' has gone down a bit, relative to the steady increase caused by the shrinking orbit.

The evolution of A_{\times}' can be understood similarly: At time t_a , the orbit is edge-on, so $H_x = 0$; also the orbit is inclined almost 45° to the arms of the detector, so the \times' detector hardly responds at all to H_+ . Thus, A_{\times}' is very small. At time t_b , the orbit's major axis is still almost 45° from the detector's arms, so the detector still responds almost solely to the principal \times mode; but now the orbit has become somewhat elliptical, thereby exciting the principal \times mode somewhat and driving A_{\times}' upward. At time t_c , the orbit is edge on, so $H_x = 0$, but now the orbit is tilted to within $45^\circ - 2\lambda_L \simeq 28^\circ$ of the nearest detector arm, so the principal $+$ mode can drive the detector significantly, thereby pushing A_{\times}' up to its maximum value. At time t_d , the orbit has tilted back to nearly 45° from the arms so only the principal \times mode can couple to the detector, and because the orbit is only slightly elliptical, that mode produces a weakened signal A_{\times}' . At t_e the orbit is edge-on so $H_x = 0$, and the orbit's major axis is still about 45° from the arms, so principal $+$ mode couples hardly at all to the detector, and A_{\times}' has become very small.

We now consider the evolution of the polarization phase $\varphi(t)$ in each of the two detectors. To deduce φ at any moment t , one need only notice how strongly each of the two wave modes (principal $+$ and principal \times) is coupled to the detector, and combine that coupling strength with a knowledge of the phase of the signal put into the detector by each mode. In doing so, one must keep in mind the overall minus signs in Eqs. (2) and (6). As one can verify from Eqs. (2)–(6) (and as might be obvious), the following is true.

(i) The polarization phase of the principal $+$ signal is zero {i.e., the signal $h(t)$ goes as $-\cos[2\Phi(t)]$ } if the orbit's major axis (i.e., the waves' principal $+$ direction) is nearer the detector's "first" arm than its "second" arm, and the phase is π {the signal goes as $+\cos[2\Phi(t)]$ } if the principal $+$ direction is nearer the second arm than

the first. (The first arm is the one that, by convention, gets stretched when $h > 0$ and squeezed when $h < 0$.)

(ii) The polarization phase of the principal \times signal is $-\pi/2$, or $3\pi/2$ {so the signal $h(t)$ goes as $-\sin[2\Phi(t)]$ } if the waves' principal \times direction is nearer the first arm than the second, and the phase is $+\pi/2$ {the signal goes as $+\sin[2\Phi(t)]$ } if the principal \times direction is nearer the second arm than the first.

Consider, as an example, the polarization phase $\varphi_{x'}$ in the x' detector. From the orbital ellipses in Fig. 22 and the above phasing rules, we deduce the following: At time t_b the principal \times mode is dominant; because the orbit is seen from below and the principal+ and principal \times axes are therefore like those of Fig. 20(c), the principal \times direction is nearly along the detector's second arm; therefore, the polarization phase is $\varphi_{x'} \simeq +\pi/2$. At time t_c only the principal+ mode is felt, and because the orbit's major axis is near the detector's first arm, the polarization phase is $\varphi_{x'} \simeq 0$. At time t_d the principal \times mode is dominant, and because the orbit is now seen from above rather than from below, its phase contribution is opposite to that at time t_b : $\varphi_{x'} \simeq -\pi/2$. At time t_e only the principal+ mode contributes, and although one cannot tell very clearly from the figure, the orbit's major axis is slightly nearer the second arm than the first, so $\varphi_{x'} = \pi$. Thus, as time passes, the polarization phase grows secularly more negative, decreasing by 2π with each orbital precession—in accord with Fig. 7(b).

4. Some useful formulas for detectors orthogonal to the waves' propagation direction

This procedure for deducing the polarization phase can be embodied in a simple and powerful diagram. As a foundation for that diagram (and as an aid for readers who might wish to explore the signal modulation more quantitatively), we shall now specialize some of the equations of the text to detectors that are orthogonal to the direction of the incoming waves. We shall deal with the same two detectors +' and x' as above and as in Sec. IV C 1 and Fig. 5, but we shall allow the binary to be precessing in any manner it wishes, and not necessarily in the simple manner of Secs. IV B and IV C.

For the +' detector with its first arm along $\hat{\mathbf{x}}$ and second along $\hat{\mathbf{y}}$, and for our underfoot source direction $\hat{\mathbf{N}} = -\hat{\mathbf{z}} + \delta\hat{\mathbf{x}}$ with $0 < \delta \ll 1$ (corresponding to $\theta = \pi - \frac{1}{2}\delta^2$ and $\phi = 0$), Eqs. (4) and (5) reduce to

$$F_+ = \cos 2\psi, \quad F_x = \sin 2\psi, \quad \psi = \arctan(\hat{\mathbf{L}}_x / \hat{\mathbf{L}}_y), \quad (A5)$$

and Eq. (3) then becomes

$$h_{+'} = h_+ \cos 2\psi + h_x \sin 2\psi. \quad (A6a)$$

This is just the real part of the standard law $h_+ + ih_{x'} = (h_+ + ih_x)e^{-i2\psi}$ by which a gravitational-wave field appears to change when one rotates one's basis axes in the plane orthogonal to the propagation direction [14], i.e., in the plane of our chosen detectors. From the imaginary

part of that law, we obtain the expression for the signal measured by our x' detector [with its first arm along $\frac{1}{2}(\hat{\mathbf{x}} + \hat{\mathbf{y}})$ and second along $\frac{1}{2}(-\hat{\mathbf{x}} + \hat{\mathbf{y}})$]:

$$h_{x'} = -h_+ \sin 2\psi + h_x \cos 2\psi. \quad (A6b)$$

In these equations, h_+ and h_x are the gravitational-wave fields (2) defined with respect to the binary's principal+ and principal \times axes. By inserting Eqs. (A5) and $\hat{\mathbf{L}} \cdot \hat{\mathbf{N}} = -\hat{\mathbf{L}}_z$ into the amplitude and phase form (7) of the measured signals, we obtain the following expressions for the precession-induced modulation of the amplitude and phase:

$$A_{+'} = \frac{2\mu M}{rD} \frac{\sqrt{(1 + \hat{\mathbf{L}}_z^2)^2 (\hat{\mathbf{L}}_y^2 - \hat{\mathbf{L}}_x^2)^2 + 16\hat{\mathbf{L}}_x^2 \hat{\mathbf{L}}_y^2 \hat{\mathbf{L}}_z^2}}}{1 - \hat{\mathbf{L}}_z^2}, \quad (A7a)$$

$$\varphi_{+'} = -\arctan\left(\frac{4\hat{\mathbf{L}}_x \hat{\mathbf{L}}_y \hat{\mathbf{L}}_z}{(1 + \hat{\mathbf{L}}_z^2)(\hat{\mathbf{L}}_y^2 - \hat{\mathbf{L}}_x^2)}\right); \quad (A7b)$$

$$A_{x'} = \frac{2\mu M}{rD} \frac{\sqrt{4(1 + \hat{\mathbf{L}}_z^2)^2 \hat{\mathbf{L}}_x^2 \hat{\mathbf{L}}_y^2 + 4\hat{\mathbf{L}}_z^2 (\hat{\mathbf{L}}_y^2 - \hat{\mathbf{L}}_x^2)^2}}}{1 - \hat{\mathbf{L}}_z^2}, \quad (A8a)$$

$$\varphi_{x'} = \arctan\left(\frac{\hat{\mathbf{L}}_z (\hat{\mathbf{L}}_y^2 - \hat{\mathbf{L}}_x^2)}{\hat{\mathbf{L}}_x \hat{\mathbf{L}}_y (1 + \hat{\mathbf{L}}_z^2)}\right). \quad (A8b)$$

These expressions can be used to verify and quantify the discussion of the previous section. More importantly, we shall now use the phase expressions to construct a powerful diagram for deducing the polarization phase modulation.

5. The cell diagram for detectors orthogonal to the propagation direction

The detector's polarization phase φ assumes the special values of $0, \pi/2, \pi$, and $3\pi/2$ whenever the binary's orbital angular momentum \mathbf{L} is oriented in one of a set of special directions relative to the detector's arms. These special orientations can be deduced equally well from Eq. (A7b) or Eq. (A8b); and they are depicted in Fig. 23. Note that the special orientations comprise boundaries or "walls" in orbital-angular-momentum space. Each wall in the figure is labeled by the value that φ assumes when \mathbf{L} lies in it. The walls with $\varphi = 0$ or π are shaded; those with $\varphi = \pi/2$ or $3\pi/2$ are white.

We shall call Fig. 23 a *cell diagram* because its walls divide the orbital-angular-momentum space into sixteen cells. The values of φ at orientations inside each cell can be deduced, roughly, by interpolation from the values on its three walls.

From the precessional motion of \mathbf{L} in this cell diagram, one can deduce directly the evolution of the polarization phase φ . Here are a few examples: If the precessional motion of \mathbf{L} encloses the intersection line between a dark

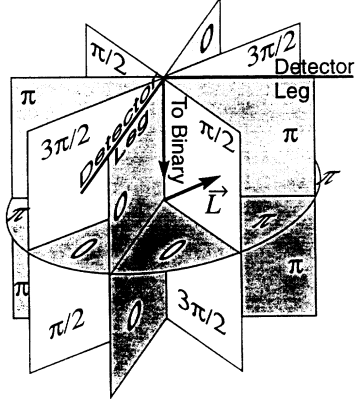


FIG. 23. The *cell diagram*, which exhibits the polarization phase φ of a detector's gravitational-wave signal as a function of the relative orientation of the detector's arms and the binary's orbital angular momentum vector \mathbf{L} .

wall and a light one, then φ will grow secularly, gaining or losing 2π with each precessional period (depending on the direction of precession). The $\varphi_{x'}$ of Fig. 7 is an example of this. If the precessional motion almost but not quite encloses such a light-dark intersection, then φ will evolve like the dotted modification of Fig. 7. If the precession encloses the vertical direction, where two light and two dark walls intersect, then φ will change secularly by $\pm 4\pi$ with each precessional period. If the precession encloses an intersection of two dark walls, then φ will oscillate up and down around zero, with two oscillations per precession period. The φ_{+} of Fig. 7 is an example of this in which the precession is barely encompassing the dark-wall intersection, so one of the two oscillations is tiny while the other is large.

It is important to keep in mind that the total phase of the signal measured by the detector is not φ , but rather $\varphi + \delta\Phi$, and that $\delta\Phi$, like φ , can grow secularly with each precession. For simple precession, that growth is embodied in Eq. (65) which, stated in words, says: For simple precession of $\hat{\mathbf{L}}$ with opening angle λ_L , if the precession cone encloses the direction $\hat{\mathbf{N}}$ to the binary, then $\delta\Phi$ changes secularly with each precession by $\Delta\delta\Phi = -2\pi \cos \lambda_L$; if the precession cone does not enclose $\hat{\mathbf{N}}$, then $\Delta\delta\Phi = 2\pi(1 - \cos \lambda_L)$ if $\cos \lambda_L > 0$ and $\Delta\delta\Phi = 2\pi(-1 - \cos \lambda_L)$ if $\cos \lambda_L < 0$.

6. Detectors not orthogonal to the propagation direction

In the last three sections we required that the detector be orthogonal to the waves' propagation direction. By doing so, we guaranteed that each of the two arms experienced precisely the same linear combination of principal+ and principal \times modes, and the net signal was just twice that for either arm by itself. If, instead, the detector is inclined to the propagation direction (i.e., if the waves do not come in from directly overhead or underfoot), then the signal in each arm is the same as it would feel if it were projected into the orthogonal plane, and the net signal is the sum of those from the two legs. The projection, unfortunately, changes the lengths of the two legs by amounts that need not be the same and changes the angle between them so it no longer need be 90° . Therefore, it is not trivial to deduce, by the diagrammatic techniques of this Appendix, the details of the net signal modulation: One must construct the equivalent, projected interferometer, then use the diagrams to deduce the signal in each leg, and then combine the signals.

-
- [1] A. Abramovici *et al.*, Science **256**, 325 (1992).
 - [2] R. Narayan, T. Piran, and A. Shemi, Astrophys. J. **379**, L17 (1991); E. S. Phinney, *ibid.* **380**, L17 (1991).
 - [3] C. Cutler, T. A. Apostolatos, L. Bildsten, L. S. Finn, E. E. Flanagan, D. Kenefick, D. M. Markovic, A. Ori, E. Poisson, G. J. Sussman, and K. S. Thorne, Phys. Rev. Lett. **70**, 2984 (1993).
 - [4] C. Cutler and E. E. Flanagan, Phys. Rev. D **49**, 2658 (1994).
 - [5] L. S. Finn and D. Chernoff, Phys. Rev. D **47**, 2198 (1993).
 - [6] C. W. Lincoln and C. M. Will, Phys. Rev. D **42**, 1123 (1990).
 - [7] E. Poisson, Phys. Rev. D **47**, 1511 (1993).
 - [8] L. E. Kidder, C. M. Will, and A. G. Wiseman, Phys. Rev. D **47**, 4183 (1993).
 - [9] R. V. Wagoner and C. M. Will, Astrophys. J. **210**, 764 (1976); **215**, 984 (1977).
 - [10] L. Blanchet and T. Damour, Ann. Inst. Henri Poincaré **50**, 377 (1989).
 - [11] T. Damour and B. R. Iyer, Ann. Inst. Henri Poincaré **54**, 115 (1991).
 - [12] L. Kidder (unpublished).
 - [13] K. Danzmann, A. Rüdiger, R. Schilling, W. Winkler, J. Hough, G. P. Newton, D. Robertson, N. A. Robertson, H. Ward, P. Bender, J. Faller, D. Hils, R. Stebbins, C. D. Edwards, W. Folkner, M. Vincent, A. Bernard, B. Bertotti, A. Brillet, C. N. Man, M. Cruise, P. Gray, M. Sandford, R. W. P. Drever, V. Kose, M. Kühne, B. F. Schutz, R. Weiss, and H. Welling, "LISA: Proposal for a Laser-Interferometer Gravitational Wave Detector in Space," Report No. MPQ 177 from the Max-Planck-Institut für Quantenoptik, 8046 Garching bei München, Germany (unpublished).
 - [14] K. S. Thorne, in *300 Years of Gravitation*, edited by S. W. Hawking and W. Israel (Cambridge University Press, Cambridge, England, 1987), p. 330.
 - [15] P. C. Peters and J. Mathews, Phys. Rev. **131**, 435 (1963).
 - [16] G. B. Cook, S. L. Shapiro, and S. A. Teukolsky, Astrophys. J. (in press).
 - [17] B. M. Barker and R. F. O'Connell, Gen. Relativ. Gravit. **11**, 149 (1979).
 - [18] K. S. Thorne and J. B. Hartle, Phys. Rev. D **31**, 1815

- (1985).
- [19] C. W. Misner, K. S. Thorne, and J. A. Wheeler, *Gravitation* (Freeman, San Francisco, 1973).
 - [20] L. Bildsten and C. Cutler, *Astrophys. J.* **400**, 175 (1992).
 - [21] D. Kennefick, D. Laurence, and K. S. Thorne (unpublished).
 - [22] B. F. Schutz, *Nature* **323**, 310 (1986); B. F. Schutz, *Class. Quantum Grav.* **6**, 1761 (1989).
 - [23] Y. Gursel and M. Tinto, *Phys. Rev. D* **40**, 3884 (1990); P. Jaranowski and A. Krolak (unpublished).
 - [24] H. D. Wahlquist, *Gen. Relativ. Gravit.* **19**, 1101 (1987).
 - [25] A. Krolak, J. A. Lobo, and B. J. Meers, *Phys. Rev. D* **43**, 2470 (1991).

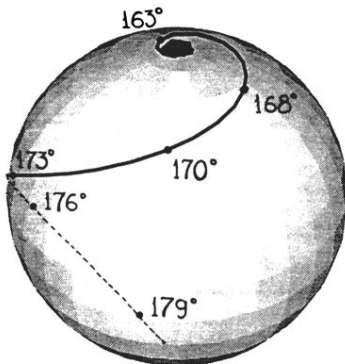


FIG. 10. The end point of transitional precession, i.e., the direction $\hat{\mathbf{J}}_f$ of the binary's total angular momentum $\hat{\mathbf{J}}$ at asymptotically late times, expressed as a function of the initial direction $\hat{\mathbf{J}}_i$ of $\hat{\mathbf{J}}$ (which is taken to be the north pole, $\theta' = 0$) and of the angle $\arccos(\kappa)$ between $\hat{\mathbf{L}}$ and $\hat{\mathbf{S}}$. The mass and spin ratios are chosen to be $M_2/M_1 = 0.2$, $S_1/M_1^2 = 1$, and $S_2 = 0$. Each point on the curve is the result of evolving the precession equations (40) from early to late times for that point's value of κ . One more piece of initial data, besides $\hat{\mathbf{J}}_i$, is needed to fully specify the evolution: the azimuthal direction of $\hat{\mathbf{J}}$ at some early, but finite, time. In this figure, $\hat{\mathbf{J}}$ is chosen to point in the direction $\phi' = 0$ at the moment when the gravity wave frequency f equals $10(M/10M_\odot)$ Hz.

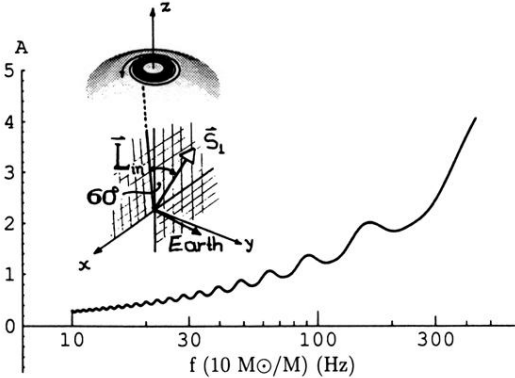


FIG. 11. This and the next seven figures (Figs. 11–18) depict the precession of the orbital angular momentum direction $\hat{\mathbf{L}}$ and the resulting modulated signal amplitude $A(t)$ in the detector, as computed by numerical integrations of the precession equations (11) together with Eqs. (19a) and (20). In all these figures the detector's legs are along the x and y axes, the direction from the detector to the binary is $\hat{\mathbf{N}} = (\hat{\mathbf{z}} + \hat{\mathbf{x}})/\sqrt{2}$, the total spin $\mathbf{S} = \mathbf{S}_1 + \mathbf{S}_2$ has magnitude $S = M_1^2$, the angle between the orbital angular momentum \mathbf{L} and the total spin \mathbf{S} is 60° so $\kappa = \hat{\mathbf{L}} \cdot \hat{\mathbf{S}} = 0.5$ (except in Figs. 17 and 18, where that angle is 178° and $\kappa = -0.99939$), and at the beginning of the integration—when $f = 10(10M_\odot/M)$ Hz, $r/M = 75$, and $L = \sqrt{75}M_1M_2$ —the total angular momentum $\mathbf{J} = \mathbf{L} + \mathbf{S}$ points in the z direction, and $\hat{\mathbf{L}}$ is in the x - z plane, on the $+x$ side of the z -axis, while $\hat{\mathbf{S}}$ is in the x - z plane, on the $-x$ side of the z -axis. When both bodies are spinning (Figs. 12, 14, 16, and 18), their spins initially lie in the $\hat{\mathbf{y}}\text{-}\hat{\mathbf{S}}$ plane. The figures differ from each other in their mass ratio M_2/M_1 and in the magnitudes of the bodies' spins. In this figure, the masses are equal, $M_2/M_1 = 1$, body 1 is maximally spinning, $S_1 = M_1^2$, and body 2 is nonspinning, $S_2 = 0$, so $\mathbf{S} = \mathbf{S}_1$ and \mathbf{L} have the initial values shown in the drawing. The subsequent motion of $\hat{\mathbf{L}}$ is shown as an outward-spiraling path on the sphere. The graph shows the amplitude $A(t)$ of the gravitational-wave signal measured by the detector.

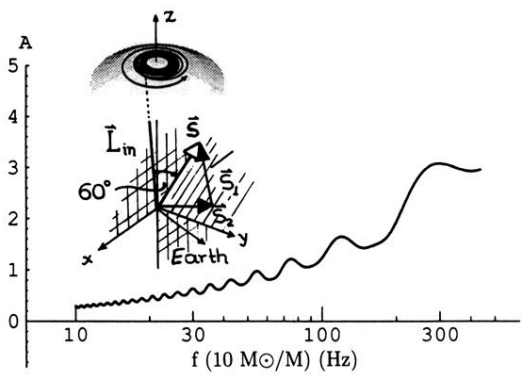


FIG. 12. Same as Fig. 11, and with the same mass ratio $M_1/M_2 = 1$ but with both bodies maximally spinning, $S_1 = M_1^2$, $S_2 = M_2^2$, so the initial \mathbf{S}_1 , \mathbf{S}_2 , \mathbf{S} , and \mathbf{L} are as shown.

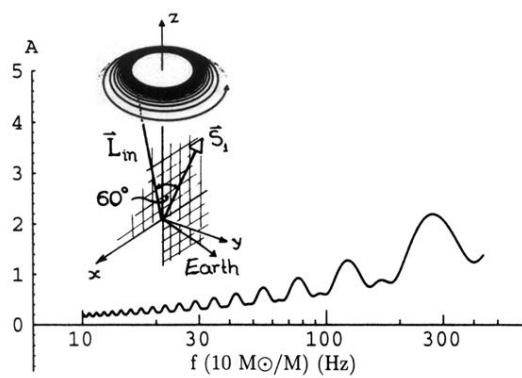


FIG. 13. Same as Fig. 11, but with $M_2/M_1 = 0.3$, $S_1 = M_1^2$ and $S_2 = 0$, so the initial \mathbf{S}_1 and \mathbf{L} are as shown.

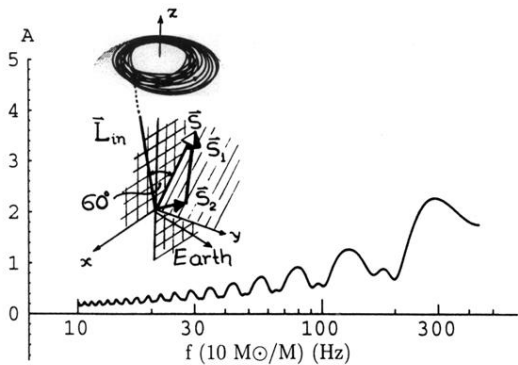


FIG. 14. Same as Fig. 11, but with $M_2/M_1 = 0.3$ (as in Fig. 13) and $S_1 = M_1^2$, $S_2 = M_2^2$, so the initial \mathbf{S}_1 , \mathbf{S}_2 , \mathbf{S} , and $\hat{\mathbf{L}}$ are as shown.

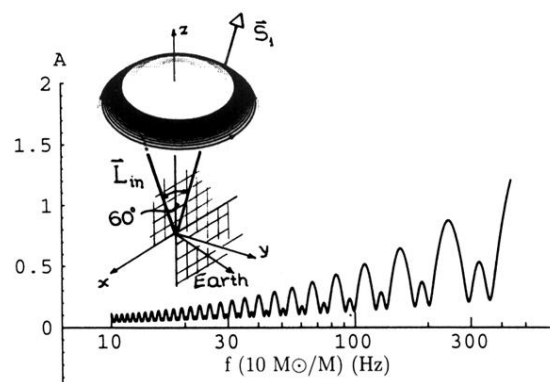


FIG. 15. Same as in Fig. 11, but with $M_2/M_1 = 0.1$, $S_1 = M_1^2$ and $S_2 = 0$, so the initial \mathbf{S}_1 and \mathbf{L} are as shown.

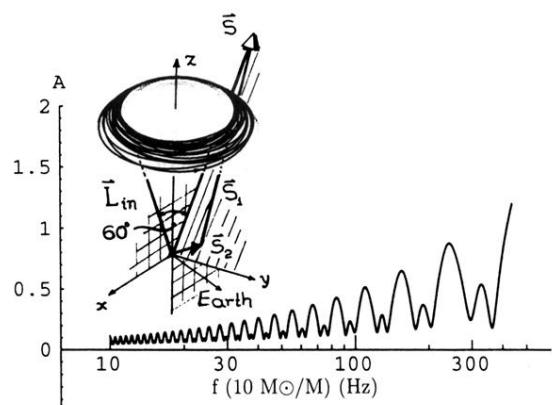


FIG. 16. Same as in Fig. 11, but with $M_2/M_1 = 0.1$ (as in Fig. 15) and $S_1 = M_1^2$, $S_2 = M_2^2$, so the initial \mathbf{S}_1 , \mathbf{S}_2 , \mathbf{S} , and $\hat{\mathbf{L}}$ are as shown.

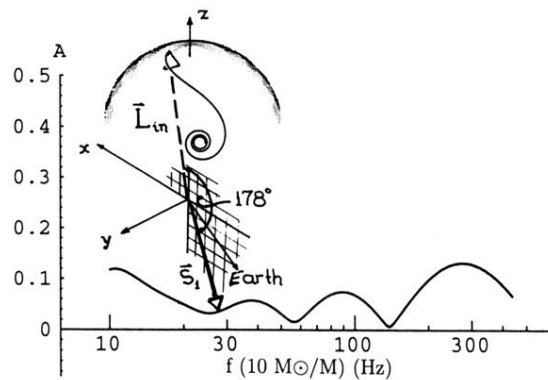


FIG. 17. Same as in Fig. 11, but with $\hat{\mathbf{L}}$ and $\hat{\mathbf{S}}$ nearly antialigned (i.e., separated by an angle of 178° so $\kappa = -0.99939$), and with $M_2/M_1 = 0.13$, $S_1 = M_1^2$, and $S_2 = 0$, so the initial \mathbf{S}_1 and \mathbf{L} are as shown. The evolution illustrates transitional precession and the subsequent return to simple precession.

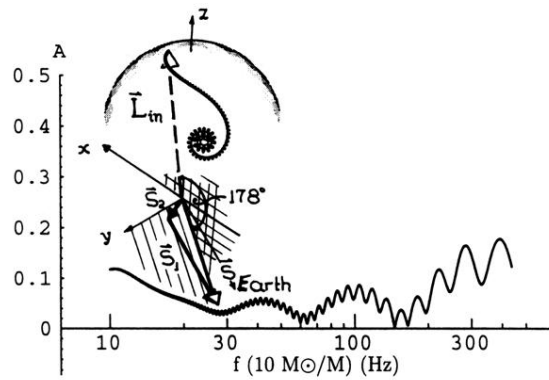


FIG. 18. Same as in Fig. 11, but with the same near antialignment and mass ratio as in Fig. 17 (angle 178° between $\hat{\mathbf{L}}$ and $\hat{\mathbf{S}}$, $\kappa = -0.99939$, $M_2/M_1 = 0.13$), and with $S_1 = M_1^2$, $S_2 = M_2^2$, so the initial \mathbf{S}_1 , \mathbf{S}_2 , \mathbf{S} , and \mathbf{L} are as shown. The evolution is essentially the same as in Fig. 17, but with visible “epicycles” due to the relatively rapid precession of \mathbf{S}_2 around \mathbf{L} .

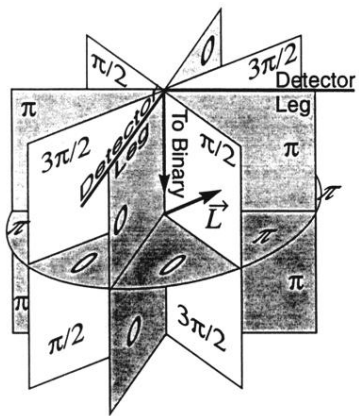


FIG. 23. The *cell diagram*, which exhibits the polarization phase φ of a detector's gravitational-wave signal as a function of the relative orientation of the detector's arms and the binary's orbital angular momentum vector \mathbf{L} .

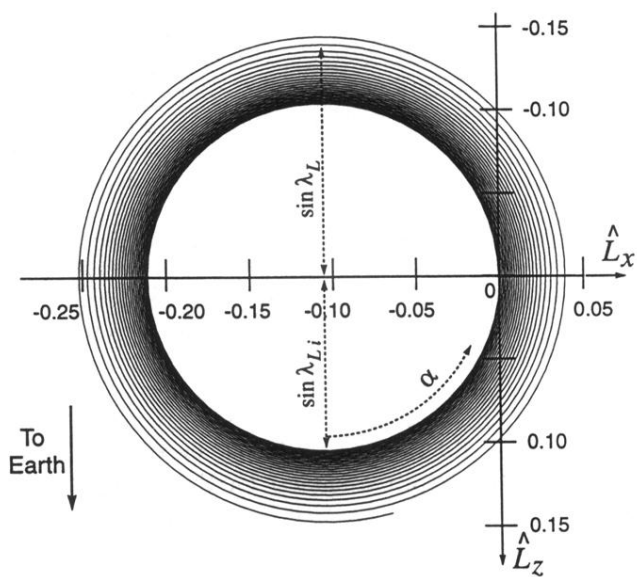


FIG. 6. The precession of $\hat{\mathbf{L}}$ (and hence also of the orbital plane) for the binary whose initial conditions are depicted in the upper left part of Fig. 5.